

**Best
Available
Copy**

AD-760 777

MATERIALS PROCESSING OF RARE EARTH-
COBALT PERMANENT MAGNETS

Paul I. Jorgensen, et al

Stanford Research Institute

Prepared for:

Air Force Materials Laboratory

February 1973

DISTRIBUTED BY:

NTIS

National Technical Information Service
U. S. DEPARTMENT OF COMMERCE
5285 Port Royal Road, Springfield Va. 22151

AFML-TR-73-60

MATERIALS PROCESSING OF RARE EARTH COBALT PERMANENT MAGNETS

P. J. Jorgensen
R. W. Bartlett

Stanford Research Institute

TECHNICAL REPORT AFML-TR-73-60

February 1973

Approved for public release; distribution unlimited.

Reproduced by
NATIONAL TECHNICAL
INFORMATION SERVICE
U S Department of Commerce
Springfield VA 22151

Air Force Materials Laboratory
Air Force Systems Command
Wright-Patterson Air Force Base, Ohio 45433




AD 760777

NOTICE

When Government drawings, specifications, or other data are used for any purpose other than in connection with a definitely related Government procurement operation, the United States Government thereby incurs no responsibility nor any obligation whatsoever; and the fact that the government may have formulated, furnished, or in any way supplied the said drawings, specifications, or other data, is not to be regarded by implication or otherwise as in any manner licensing the holder or any other person or corporation, or conveying any rights or permission to manufacture, use, or sell any patented invention that may in any way be related thereto.

Copies of this report should not be returned unless return is required by security considerations, contractual obligations, or notice on a specific document.

ACCESSION for	
HTIS	White Section <input checked="" type="checkbox"/>
DOC	Buff Section <input type="checkbox"/>
UNANNOUNCED	<input type="checkbox"/>
JUSTIFICATION	
BY	
DISTRIBUTION/AVAILABILITY CODES	
Dist.	A. MIL. RES/ST. SP. CIAL
	

UNCLASSIFIED

Security Classification

DOCUMENT CONTROL DATA - R & D

Security classification of title, body of abstract and indexing annotation must be entered when the overall report is classified.

1. ORIGINATING AGENCY (Corporate author) Stanford Research Institute 333 Ravenswood Avenue Menlo Park, California 94025		2a. REPORT SECURITY CLASSIFICATION UNCLASSIFIED	
3. REPORT TITLE MATERIALS PROCESSING OF RARE EARTH-COBALT PERMANENT MAGNETS			
4. DESCRIPTIVE NOTES (Type of report and inclusive dates)			
5. AUTHOR(S) (First name, middle initial, last name) Paul J. Jorgensen Robert W. Bartlett			
6. REPORT DATE February 1973	7a. TOTAL NO. OF PAGES 74	7b. NO. OF REFS 24	
8a. CONTRACT OR GRANT NO. F33615-70-C-1624	9a. ORIGINATOR'S REPORT NUMBER(S) PYU-8731		
b. PROJECT NO. ARPA Order No. 1617	9b. OTHER REPORT NUMBER(S) (Any other numbers that may be assigned this report)		
c. Program Code No. OD10	AFML-TR-73-60		
10. DISTRIBUTION STATEMENT Approved for public release; distribution unlimited.			
11. SUPPLEMENTARY NOTES		12. SPONSORING MILITARY ACTIVITY Air Force Materials Laboratory Wright Patterson Air Force Base Ohio 45433	
13. ABSTRACT <p>A study of the oxidation kinetics of SmCo_5 involving selective oxidation of samarium was extended from high temperatures to 100°C without a change in the diffusion-controlled rate mechanism. The low temperature oxidation rates are consistent with the amount of oxidation normally observed in SmCo_5 powders and with the temperature rise expected from oxidation of ground powders. The solubility of oxygen in SmCo_5 at 1130°C (sintering temperature) in excess of the 800°C solubility was determined to be 3500 ± 500 ppm. The source of oxygen during sintering is the oxide subscale. Sub-micron oxide particles precipitate within the SmCo_5 grains on cooling from the sintering temperature. Oxidation causes depletion of samarium and precipitation of $\text{Sm}_2\text{Co}_{17}$ particles within grains. Both inclusions are postulated to be sources of domain wall nucleation. The oxide inclusions can be removed at 800°C by an aging treatment, that collects the oxide into a few large grains outside the SmCo_5 grains by a solution-reprecipitation mechanism involving grain boundary transport of samarium. The $\text{Sm}_2\text{Co}_{17}$ inclusions are not affected by thermal aging, but they can be prevented from occurring by including excess samarium in the sintered compact to replenish samarium lost by oxidation.</p> <p>The kinetics of solid phase sintering of SmCo_5 have been studied as a function of time, temperature, and stoichiometry. The kinetics can be described by a grain boundary transport mechanism that is independent of the samarium/cobalt ratio in the alloy.</p>			

DD FORM 1473

(PAGE 1)

S/N 0101-807-6801

1 a

UNCLASSIFIED

Security Classification

UNCLASSIFIED

Security Classification

14 KEY WORDS	LINK A		LINK B		LINK C	
	ROLE	WT	ROLE	WT	ROLE	WT
Magnetic Particles						
Rare Earth						
Cobalt						
Oxidation						
Internal-Oxidation						
Sintering						
Diffusion						
Magnetic-coercivity						

MATERIALS PROCESSING OF RARE EARTH COBALT PERMANENT MAGNETS

P. J. Jorgensen
R. W. Bartlett

Approved for public release; distribution unlimited.

FOREWORD

This is the fifth semiannual interim technical report of the research program "Materials Processing of Rare Earth-Cobalt Permanent Magnets" under Contract F33615-70-C-1624. Stanford Research Institute project number is PYU-8731. This project is being conducted by the Materials Laboratory of Stanford Research Institute. Dr. Paul J. Jorgensen, Manager of the Ceramics Group, is the project supervisor. Dr. Robert W. Bartlett of Stanford University is project consultant. The research described in this report is part of the contractual research program of the Electromagnetic Materials Division, Air Force Materials Laboratory, Air Force Systems Command, Wright-Patterson AFB, Ohio. Mr. Harold J. Garrett (AFML/LPE) is the project monitor. It was sponsored by the Advanced Research Project Agency, ARPA Order No. 1617, Program Code No. OD10.

This report covers research conducted between July 1 and December 31, 1972 and was submitted in February 1973 by the authors for publication.

This technical report has been reviewed and is approved.



CHARLES H. ROBISON, Major, USAF
Chief, Solid State Materials Branch
Electromagnetic Materials Division
Air Force Materials Laboratory

ABSTRACT

A study of the oxidation kinetics of SmCo_5 involving selective oxidation of samarium was extended from high temperatures to 100°C without a change in the diffusion-controlled rate mechanism. The low temperature oxidation rates are consistent with the amount of oxidation normally observed in SmCo_5 powders, and with the temperature rise expected from oxidation of ground powders. The solubility of oxygen in SmCo_5 at 1130°C (sintering temperature) in excess of the 800°C solubility was determined to be 3500 ± 500 ppm. The source of oxygen during sintering is the oxide subscale. Submicron oxide particles precipitate within the SmCo_5 grains on cooling from the sintering temperature. Oxidation causes depletion of samarium and precipitation of $\text{Sm}_2\text{Co}_{17}$ particles within grains. Both inclusions are postulated to be sources of domain wall nucleation. The oxide inclusions can be removed at 800°C by an aging treatment, that collects the oxide into a few large grains outside the SmCo_5 grains by a solution/reprecipitation mechanism involving grain boundary transport of samarium. The $\text{Sm}_2\text{Co}_{17}$ inclusions are not affected by thermal aging, but they can be prevented from occurring by including excess samarium in the sintered compact to replenish samarium lost by oxidation.

The kinetics of solid phase sintering of SmCo_5 have been studied as a function of time, temperature, and stoichiometry. The kinetics can be described by a grain boundary transport mechanism that is independent of the samarium/cobalt ratio in the alloy.

CONTENTS

I	INTRODUCTION	1
II	OXIDATION OF SmCo_5	3
A.	Oxidation, Subscale Structure, and Composition	3
B.	Kinetics of Internal Oxidation of SmCo_5 at Elevated Temperatures	5
C.	Kinetics of Oxidation at Low Temperatures	8
D.	Expected Temperature Rise Associated with Low Temperature Oxidation	14
E.	Oxidation Rate Mechanism	16
III	VACUUM ANNEALING PARTIALLY OXIDIZED SmCo_5 AT SINTERING TEMPERATURES	25
IV	OXYGEN SOLUBILITY DURING SINTERING AND SUBSEQUENT OXIDE PRECIPITATION IN SmCo_5	31
V	PRECIPITATION OF $\text{Sm}_2\text{Co}_{17}$ IN SmCo_5	39
VI	DISCUSSION OF Sm_2O_3 AND $\text{Sm}_2\text{Co}_{17}$ INCLUSIONS AND INTRINSIC COERCIVITY IN SINTERED MAGNETS	43
A.	Summary of Inclusions	43
B.	Inclusions and Intrinsic Coercivity	43
VII	SINTERING	
A.	Introduction	49
B.	Experimental Procedure	51
C.	Results and Discussion	52
	REFERENCES	63

ILLUSTRATIONS

1	Coarse Fibrous Structure of Samarium Oxide in the Oxide/ Cobalt Composite Subscale Grown at High Temperatures, 1150°C	4
2	X-Ray Diffraction Spectra for the Oxide Subscales Grown in Air and in Pure Oxygen	6
3	Arrhenius Plot for the Internal Oxidation Rate at High Temperatures	7
4	Oxygen Dissociation Pressures for CoO in a 90% CO ₂ + 10% CO Mixture	9
5	Internal Oxidation Rate Dependence on Oxygen Pressure (Air Equilibrium at Surface)	10
6	Internal Oxidation Rate Dependence on Oxygen Pressure (CoO Equilibrium at Surface)	11
7	Thermogravimetric Data for Internal Oxidation of 25 μm SmCo ₅ Particles	13
8	Arrhenius Plot for the Internal Oxidation Rate Extended to Lower Temperatures	15
9	Adiabatic Temperature Rise Accompanying Partial Oxidation to Sm ₂ O ₃	17
10	Oxygen Self-Diffusion in B-Type Sm ₂ O ₃ (After Stone ⁶)	19
11	Fibrous Samarium Oxide with a Crack in the Subscale Grown at 800°C	22
12	Oxide Depletion Zone Resulting from Internal Oxidation of SmCo ₅ Followed by Vacuum Annealing, 125X	26
13	Oxide Depletion Zone at Higher Magnification (SEM)	27
14	Boundary of the Oxide Depleted Zone (Right Side) Within the Subscale	28

ILLUSTRATIONS (Concluded)

15	Boundary Between the Oxide Depleted Zone and the SmCo_5 Core	30
16	Oxide Precipitates in the SmCo_5 Grains after Oxygen Saturation at 1125°C and Aging at 800°C	33
17	Quenched and Aged SmCo_5 Grains	35
18	Samarium Oxide Particles in a Sintered SmCo_5 Magnet Uncovered by Etching	37
19	Scanning Electronmicrograph of $\text{Sm}_2\text{Co}_{17}$ Precipitates in SmCo_5	40
20	Magnetic Domains Passing Through $\text{Sm}_2\text{Co}_{17}$ Precipitates Within SmCo_5 Grains	46
21	Linear Thermal Expansion of Polycrystalline Randomly Oriented SmCo_5	53
22	Samarium-Cobalt Shrinkage Isotherms for an Alloy Containing 27.7 wt% Sm	54
23	Samarium-Cobalt Shrinkage Isotherms for an Alloy Containing 31.35 wt% Sm	55
24	Samarium-Cobalt Shrinkage Isotherms for Alloys Containing 33.0 and 33.33 wt% Sm	56
25	Arrhenius Plot of the Shrinkage Rate Versus Reciprocal Temperature	58

TABLES

1	Some Effects Involving Magnetic Coercivity in SmCo_5 and Their Possible Causes	47
2	Sintering Constants for Equation 4	50
3	Oxygen Analysis of SmCo_5 Alloys	59

I INTRODUCTION

The objectives of this program are to investigate materials processing methods with the goal of achieving optimum properties of SmCo_5 and other RECo_5 compounds as permanent magnets. The primary problem is achieving high magnetic coercivity.

Previous to this research period, a variety of unconventional processes for generating RECo_5 powders were investigated but none was found to be more effective in obtaining high coercivity materials than the properly conducted comminution process of ball milling.

The sintering process is also a critical step in magnet production. Studies to gain further knowledge of the liquid-phase sintering process and magnetic evaluation of sintered alloys were carried out prior to this research period, and studies of the final stage of sintering (solid-state process) were conducted during this period and are reported.

Selective internal oxidation of samarium invariably accompanies magnet powder processing. A study of the kinetics of oxidation and the morphology of the oxide subscale was completed during this period. Studies on oxygen solubility in SmCo_5 and the precipitation of oxide inclusions during quenching and aging are reported.

A study of $\text{Sm}_2\text{Co}_{17}$ precipitation in samarium-depleted SmCo_5 grains is included in this report.

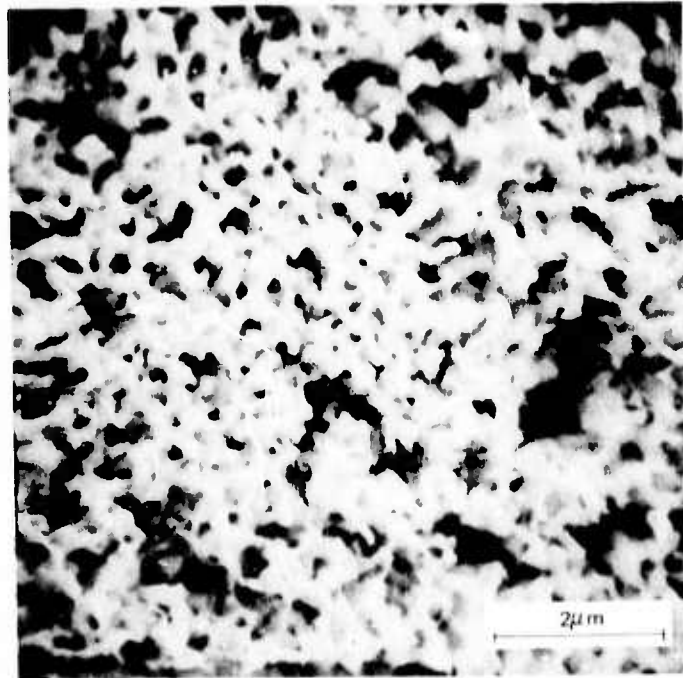
II OXIDATION OF SmCo_5

A. Oxidation, Subscale Structure, and Composition

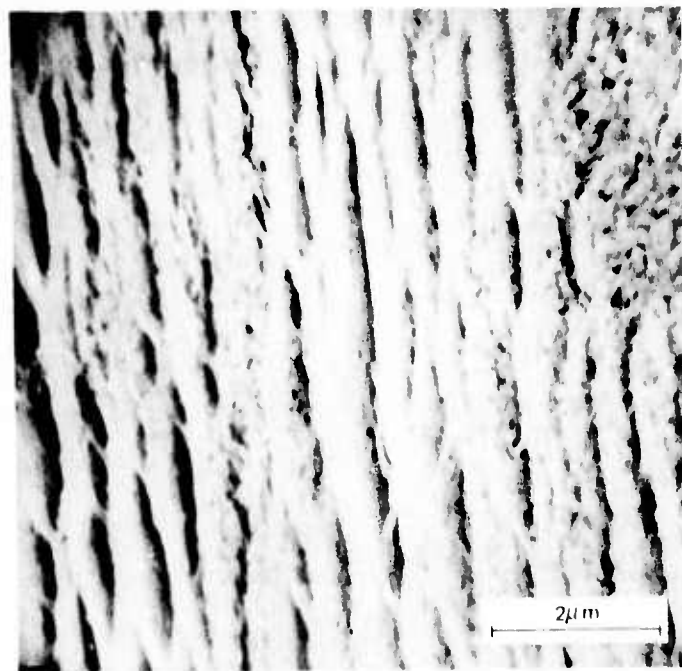
Oxidation of SmCo_5 is selective, resulting in a subscale consisting of samarium oxide platelets and fibers surrounded by cobalt. The oxide fibers are oriented in their growth direction, which is generally normal to the alloy surface. Scanning electron micrographs on the subscale structure in the direction of growth and transverse to the direction of growth are shown in Figure 1. These specimens were oxidized at 1150°C for two minutes in a 90% CO_2 + 10% CO mixture, which prevents any oxidation of cobalt. After metallographic mounting, the specimens were etched in 50% HNO_3 + 30% H_2SO_4 + 20% H_2O and vapor coated with a gold-platinum alloy. The etching removes cobalt and leaves the oxide structure in relief. The transverse section indicates that the oxide consists of fibers, narrow platelets, and a loosely interconnected network of joined platelets.

Previous x-ray diffraction determinations regarding the crystallographic structure of the composite subscale formed by internal oxidation of SmCo_5 have been somewhat confusing. More detailed x-ray diffraction studies following oxidation have now been completed on both powder samples and flat surfaces of SmCo_5 ingots. These studies have been made in pure oxygen, in air, and in the 90% CO_2 + 10% CO mixture. Determinations have been made on samples oxidized at temperatures from 320 to 1000°C . In all cases the primary metal produced is β -cobalt (cubic).

The samarium oxide phase that is obtained during oxidation is either Sm_2O_3 or an oxynitride depending on the presence or absence of nitrogen. B-type Sm_2O_3 (monoclinic) is produced at all oxidation temperatures. Pure Sm_2O_3 exhibits the monoclinic structure above $850\text{--}900^\circ\text{C}$, and C-type Sm_2O_3



(a) TRANSVERSE



(b) LONGITUDINAL

TA-8731-87

FIGURE 1 COARSE FIBROUS STRUCTURE OF SAMARIUM OXIDE IN THE OXIDE/COBALT COMPOSITE SUBSCALE GROWN AT HIGH TEMPERATURES, 1150°C

(cubic) is usually observed at lower temperatures.¹ X-ray diffraction peak intensities for the C-type sesquioxide are very weak or nonexistent. No other samarium oxide phases are observed in the absence of nitrogen.

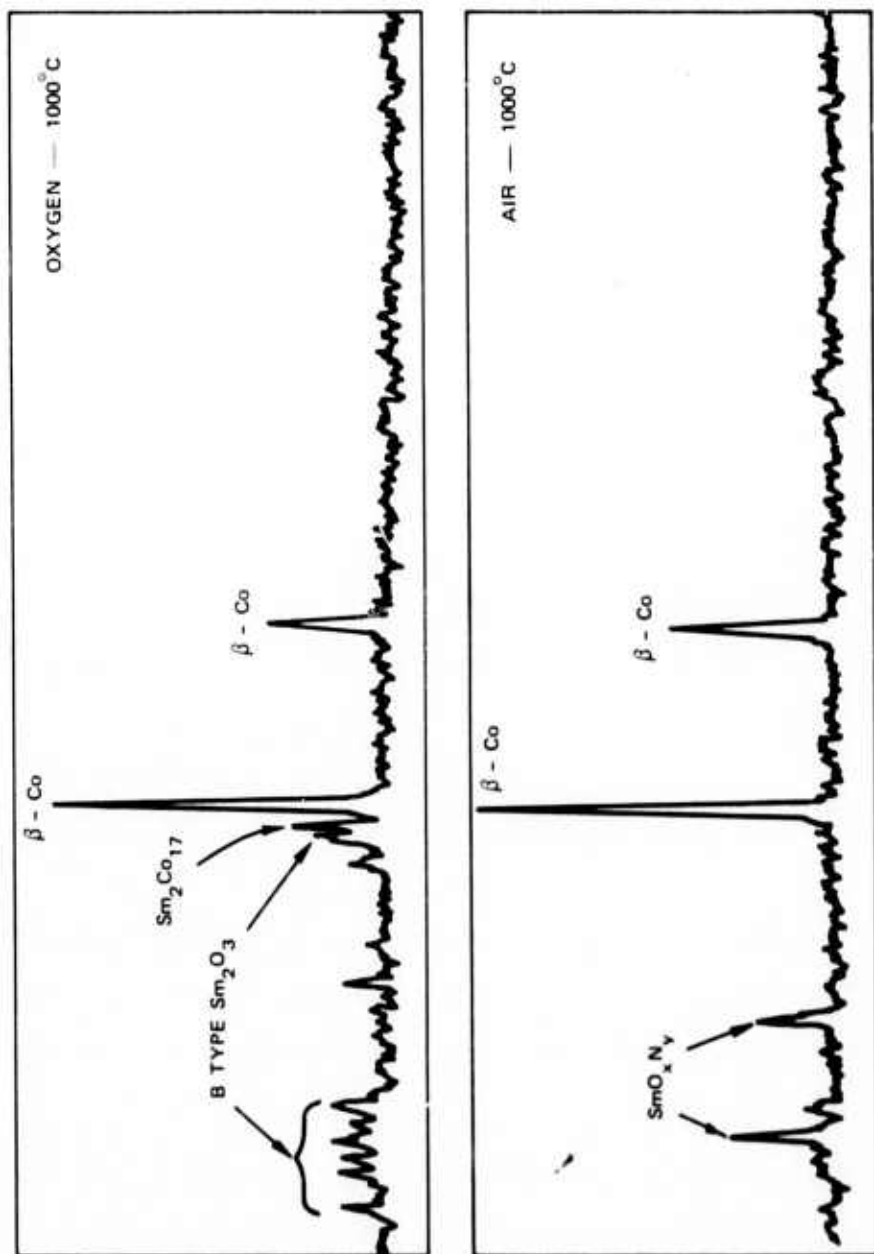
After oxidation in air, a suboxynitride phase, $\text{SmN}_{1-x}\text{O}_x$ (NaCl structure), is observed and the Sm_2O_3 peaks are weak. This samarium compound has been previously prepared and identified by Felmlee and Eyring.² Electron-beam microprobe (EBM) analyses on air-oxidized samples have indicated that the actual oxygen content of the subscale is somewhat less than that required stoichiometrically for Sm_2O_3 and somewhat greater than that required stoichiometrically for SmO . This finding is consistent with the presence of both the sesquioxide and suboxynitride. However, nitrogen was not detected by EBM analysis.

X-ray diffraction spectra taken after oxidation of subscale at 1000°C in air and oxygen are shown in Figure 2. The shift from the sesquioxide to the suboxynitride caused by nitrogen in the air oxidation tests is clearly evident.

B. Kinetics of Internal Oxidation of SmCo_5 at Elevated Temperatures

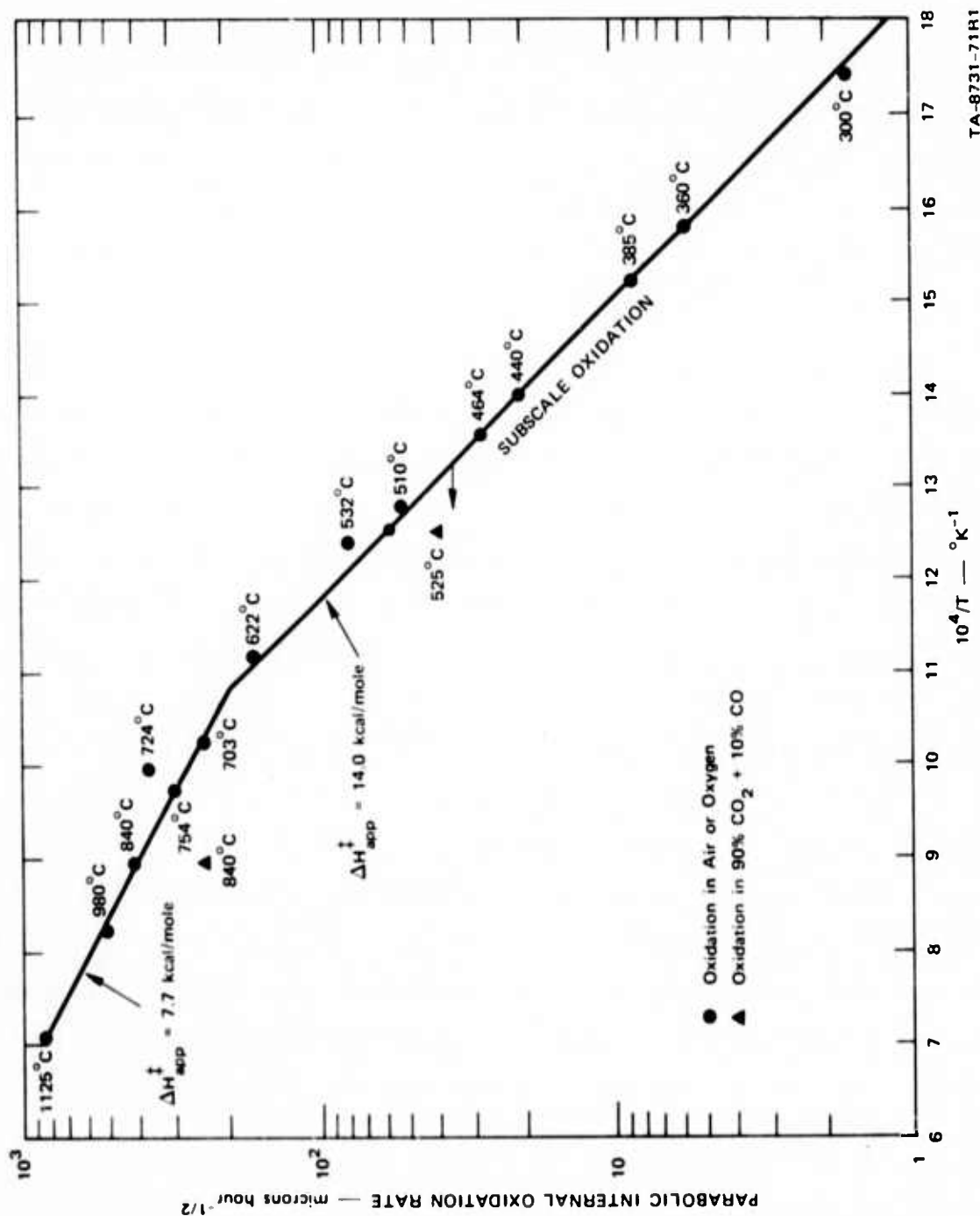
The oxide subscale thickness increases parabolically with time indicating a diffusion-controlled rate-process.³ The kinetics of this process for both SmCo_5 and PrCo_5 are identical and have been studied at elevated temperatures using a metallographic technique on small sectioned cast pieces.

The temperature dependence of the internal oxidation rate follows the Arrhenius law. Further work at higher temperatures conducted during this period has shown that there is a break in the Arrhenius plot, with a lower apparent activation energy for the oxidation rate at higher temperatures. The break in the curve occurs at about 650°C (see Figure 3). The apparent activation energies are 14.0 kcal/mole at lower temperatures



TA-8731-88

FIGURE 2 X-RAY DIFFRACTION SPECTRA FOR THE OXIDE SUBSCALES GROWN IN AIR AND IN PURE OXYGEN



TA-8731-71H1

FIGURE 3 ARRHENIUS PLOT FOR THE INTERNAL OXIDATION RATE AT HIGH TEMPERATURES

and 7.7 kcal/mole at higher temperatures. Each datum point shown in Figure 3 represents a triplicate set of runs.

With two exceptions, all the data shown in Figure 3 are from runs conducted in one atmosphere of air or oxygen. The remaining two data points were obtained from runs conducted in a flowing gas mixture of 90% CO_2 + 10% CO. The chemical potential of oxygen in this gas mixture is below that required for oxidation of cobalt; see Figure 4. Consequently, the usual thin oxide scale containing cobalt oxide over the subscale is not formed.

The markedly reduced oxygen potential in the 90% CO_2 + 10% CO mixture caused a small decrease in the subscale oxidation kinetics at 840°C and at 525°C. In both cases the rates were reduced to about half the respective rates obtained at the same temperatures in air. As determined from these limited data, the parabolic oxidation rate dependence on oxygen partial pressure is summarized in Figures 5 and 6. If the exterior samarium oxide in the subscale is in equilibrium with air at one atmosphere, then the increase in the parabolic rate constant with oxygen pressure is shown by Figure 5. However, if the exterior samarium oxide in the subscale formed by air oxidation is assumed to be in equilibrium with CoO, the oxygen pressure dependence is shown by Figure 6. In both cases the oxygen pressure dependence is very weak. Generally for parabolic oxidation of metals, it is related to the point-defect transport mechanism in the oxide. Although not enough is known about the defect mechanism in rare earth sesquioxides to draw firm conclusions, the observed oxygen pressure dependence is less than that encountered for any of the usual defect mechanisms responsible for ion diffusion in sesquioxides.

C. Kinetics of Oxidation at Low Temperatures

Ordinarily, the oxidation of magnet powders occurs during handling at room temperature, or at slightly elevated temperatures resulting from

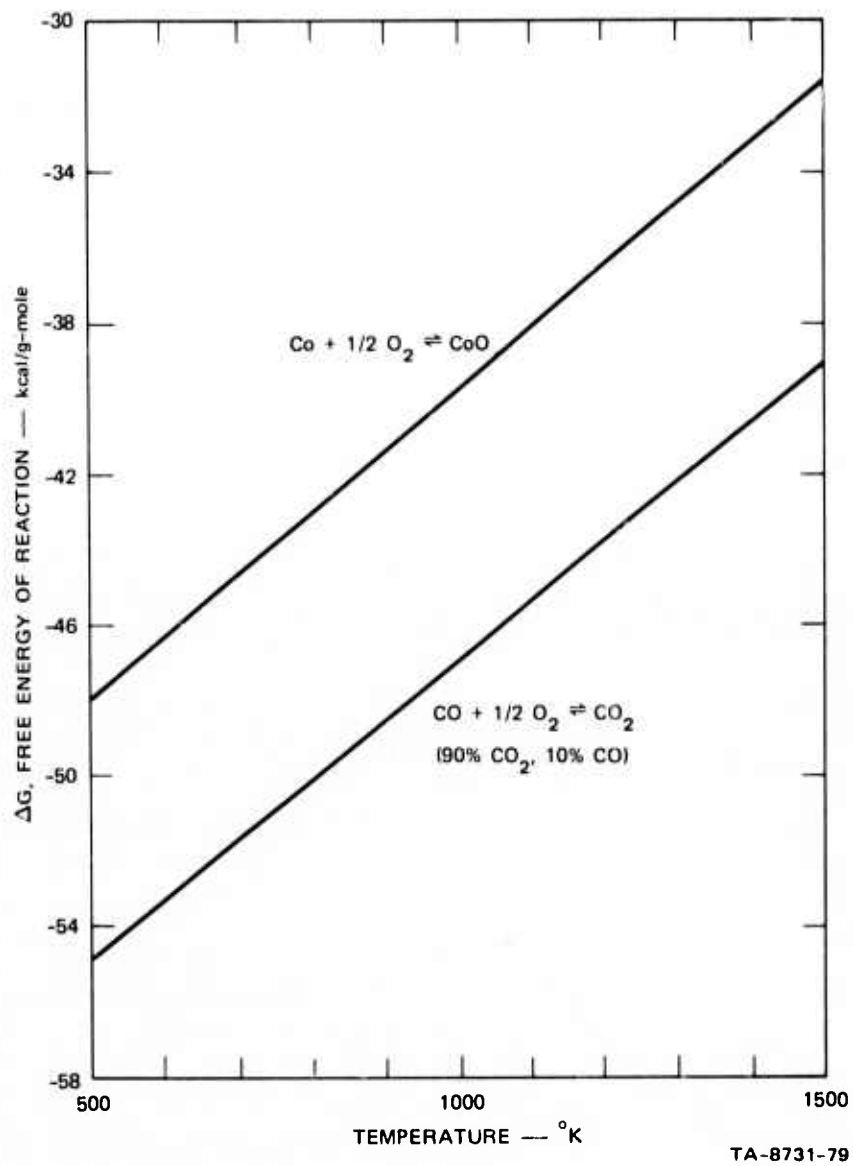


FIGURE 4 OXYGEN DISSOCIATION PRESSURES FOR CoO IN A 90% CO_2 + 10% CO MIXTURE

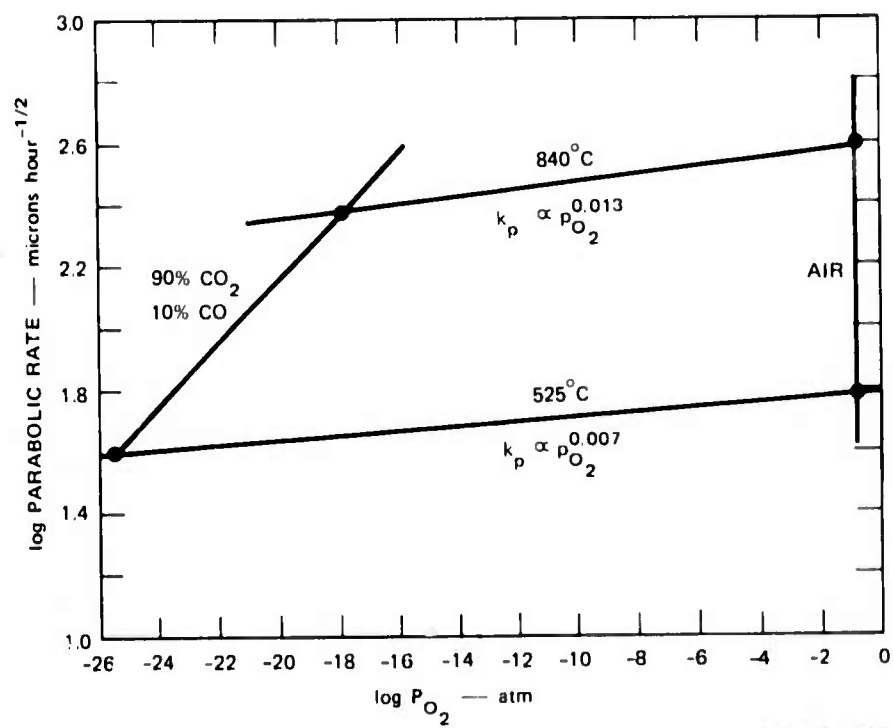
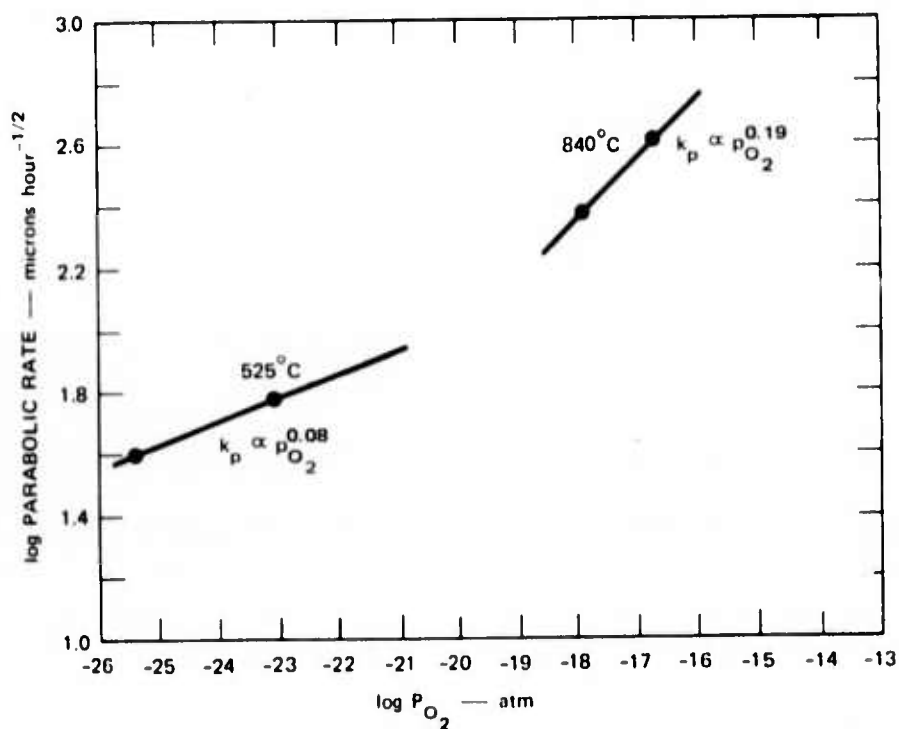


FIGURE 5 INTERNAL OXIDATION RATE DEPENDENCE ON OXYGEN PRESSURE (AIR EQUILIBRIUM AT SURFACE)



TA-8731-80R

FIGURE 6 INTERNAL OXIDATION RATE DEPENDENCE ON OXYGEN PRESSURE (CoO EQUILIBRIUM AT SURFACE)

the exothermic oxidation reaction. Therefore, it is particularly important that kinetic data be obtained at very low temperatures so that the extent of oxidation as a function of particle size, time, and temperature can be predicted. Previous attempts to measure small amounts of oxidation using a zirconia electrochemical cell, which is very sensitive to small amounts of oxygen consumption at low oxygen pressures, have been reported but the results were not very satisfactory.³ A review of these data after accumulating more knowledge about oxidation at higher temperature indicates that the majority of these runs represent measurements in such small amounts of oxygen that adsorption and desorption effects were probably dominant. As a consequence, additional oxidation kinetic studies with the zirconia cell apparatus have been conducted in higher oxygen pressures, although the oxygen pressure is still sufficiently low that differences in oxygen pressure can be measured and used to determine the oxidation kinetics below 200°C.

An electronic microbalance has been used to measure the oxidation kinetics gravimetrically in the temperature range from 150 to 250°C. The thermogravimetric data are shown in Figure 7.

For both the gravimetric and oxygen consumption methods, the results have been obtained using a single batch of SmCo_5 particles with an average particle diameter of 25 micrometers. This diameter was determined by photographing and measuring numerous particles and then averaging the diameter. In these experiments the extent of oxidation was limited to an oxide scale thickness very much smaller than the particle radius. Consequently, one dimensional planar diffusion was an adequate approximation in calculating the diffusion-controlled oxidation rate.

The weight gain and oxygen consumption curves obtained from these experiments were parabolic. The results were converted into equivalent oxide scale thickness rates for comparison with the oxide scale thickness rates determined by the sectioning technique used at higher temperatures.

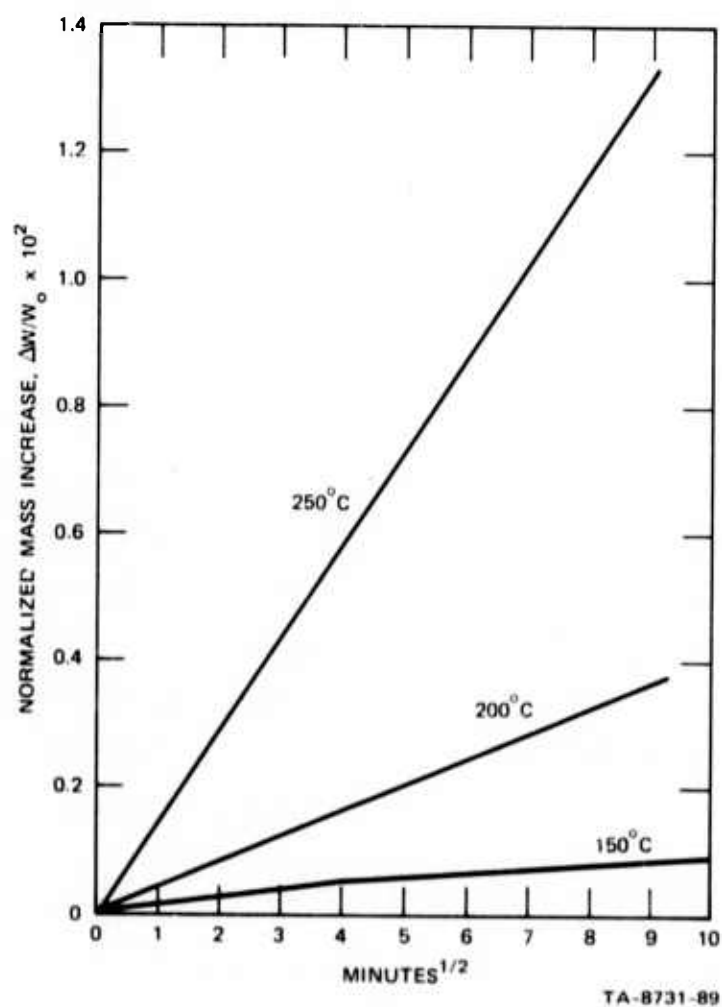


FIGURE 7 THERMOGRAVIMETRIC DATA FOR INTERNAL OXIDATION OF 25- μm SmCo_5 PARTICLES

The parabolic oxidation rates for the low temperature experiments are shown in Figure 8. The straight line is an extrapolation of the Arrhenius plot from the high temperature data of Figure 3. These data show that the same oxidation mechanism observed at higher temperatures continues down to the lowest temperature at which rates can be measured, 100°C. The kinetics for the oxidation process shown in both Figures 3 and 8 span a range of oxidation rates that is seven orders of magnitude, between 100°C and 1125°C.

D. Expected Temperature Rise Associated with Low Temperature Oxidation

The adiabatic temperature rise caused by partial oxidation of SmCo_5 has been calculated. However, the assumptions for this calculation need to be emphasized. First, samarium is selectively oxidized to samarium sesquioxide and hence all of the measured oxygen in a sample can be assigned to Sm_2O_3 . Second, the sensible heat of oxidation is uniformly distributed in the alloy particle instantaneously; rapid heat transfer occurs in the metal and the particle surface temperature, where oxidation takes place, is no greater than the interior temperature. This approximation is probably adequate for a moderately slow oxidation process and small particles such as those involved in preparing sintered magnets. The third assumption is that no heat is lost from the oxidizing metal system; the aggregate alloy powder is an adiabatic system. This approximation is probably valid for a large volume of particles and oxidation occurring fast enough that heat transfer out of the crucible or particle container is not significant.

The temperature rise will be proportional to the amount of oxygen, the specific heat of SmCo_5 , and the heat of formation of Sm_2O_3 . The specific heat is $0.1 \text{ cal g}^{-1} \text{ deg}^{-1}$, which was estimated from an assumption that the heat capacity is $7 \text{ cal g-atom}^{-1} \text{ deg}^{-1}$. The heat of formation of Sm_2O_3 at 298°K is 433,900 cal/mole.⁴

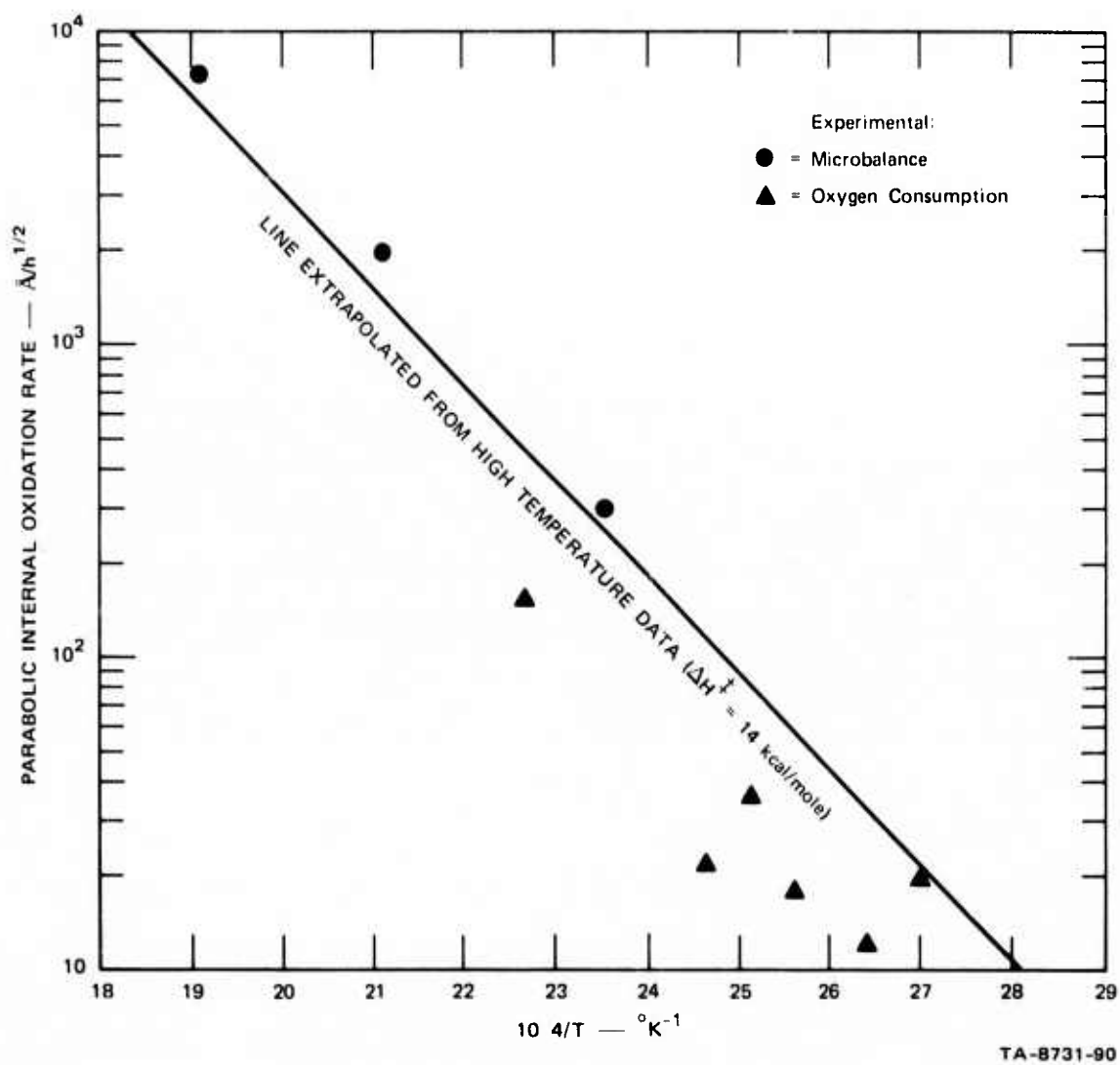


FIGURE 8 ARRHENIUS PLOT FOR THE INTERNAL OXIDATION RATE EXTENDED TO LOWER TEMPERATURES

The temperature rise caused by an increase in oxygen is shown in Figure 9. An increase of 1000 ppm of oxygen causes an adiabatic temperature increase of nearly 100°C.

As previously discussed,⁵ oxygen analyses in samarium cobalt materials after grinding generally range from a few hundred to a few thousand ppm depending on the processing and particle size. This amount of oxygen is sufficient to account for an appreciable adiabatic temperature rise during oxidation. A 100°C rise in temperature from 25 to 125°C is sufficient to account for a subscale thickness of about 100 Å in a few hours. Furthermore, a 100 Å subscale thickness is equivalent to a 1000-ppm oxygen increase for a 3-micrometer-diameter SmCo_5 particle.* Hence, for the particle sizes employed in sintered magnets, the observed increase in oxygen is consistent with the particle size, the expected temperature rise, the kinetics of oxidation, and the expected subscale thickness as a result of the temperature rise. Although these relationships do not prove that a temperature rise and the internal oxidation by the diffusion-controlled mechanism have occurred to match the observed oxygen concentration, they at least show that all of the observed results are compatible.

E. Oxidation Rate Mechanism

It was previously shown³ that the published data on the oxygen solubility in cobalt coupled with the rapid rate of internal oxidation required that the diffusion coefficient for oxygen in cobalt would have to be $1 \times 10^{-6} \text{ cm}^2/\text{sec}$ at 420°C and even greater at higher temperatures. In fact, at high temperatures the diffusion coefficient must be greater than those typically encountered for liquid metals (10^{-4} to $10^{-6} \text{ cm}^2/\text{sec}$). Consequently, it appeared that the transport of oxygen in the β -cobalt matrix could not adequately explain the rapid rate of growth of the subscale.

* See Figures 27 and 28 of Reference 3.

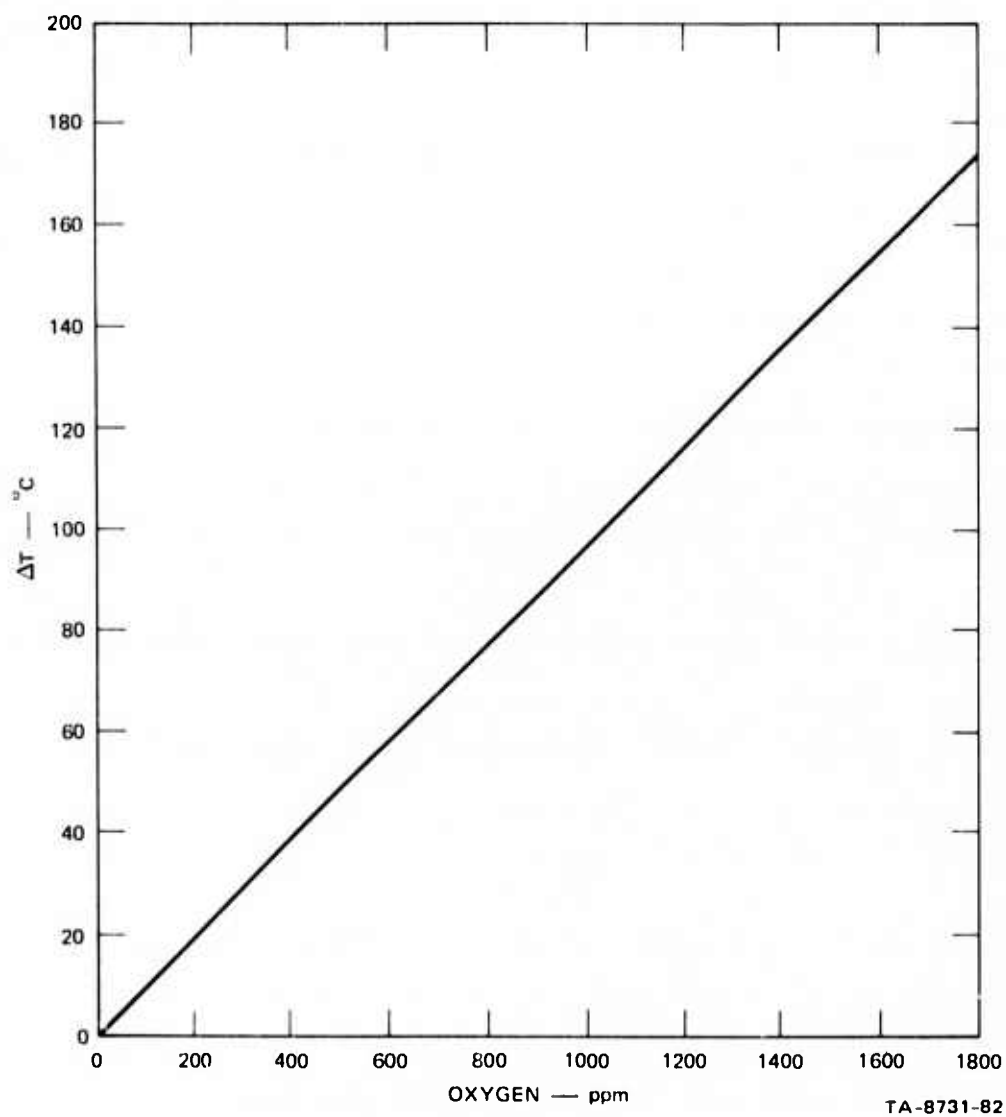


FIGURE 9 ADIABATIC TEMPERATURE RISE ACCOMPANYING PARTIAL
OXIDATION TO Sm_2O_3

A literature search to determine the available information on diffusion of oxygen in B-type and C-type rare earth sesquioxides has been made and it presently appears that oxygen anion transport within the oxide fibers is also too slow to account for the rapid growth of the subscale. Kofstad provides an adequate review of the existing diffusion literature¹ for the rare earth oxides.

A study of self-diffusion of oxygen in B-type Sm_2O_3 has been made by Stone⁶ over a temperature range between 696 and 907°C using an isotopic exchange experimental technique. The activation energy for diffusion was about 23 kcal/mole, and the data are summarized in Figure 10. Wirkus, Berard, and Wilder^{7,8} have reoxidized partially reduced rare earth sesquioxides, and although they have not studied Sm_2O_3 , they have obtained diffusion coefficients of the same order of magnitude in the same temperature ranges as the diffusion coefficients determined by Stone. Their implicit assumption is that these oxides are semiconductors, whereas Tare and Schmalzried⁹ find them to be ionic conductors at low oxygen pressures (C-type structure). At 800°C the diffusion coefficient of oxygen in Eu_2O_3 determined by Wirkus and Wilder is $D_0 = 2.27 \times 10^{-10} \text{ cm}^2 \text{ sec}^{-1}$. The value obtained from Stone's data for oxygen diffusion in Sm_2O_3 at 800°C is $D_0 = 2.76 \times 10^{-10} \text{ cm}^2 \text{ sec}^{-1}$.

If the rate of internal oxidation of SmCo_5 is determined by the flux of oxygen anions through Sm_2O_3 platelets, then one can deduce the product $D_0 \Delta C$ from the parabolic rate constant. It is instructive to make this calculation on the assumption that oxygen transport through the oxide is rate-controlling at 800°C, and compare the results with the diffusion data at the same temperature. The derived value of $D_0 \Delta C$ using this hypothesis is $1.67 \times 10^{-7} \text{ g cm sec}^{-1}$. Matching the value for the diffusion coefficient determined by Stone, namely $D_0 = 2.76 \times 10^{-10} \text{ cm}^2 \text{ sec}^{-1}$, would require an oxygen concentration difference of about 1000 g/cm^3 . This conclusion is clearly absurd since the total oxygen concentration is only

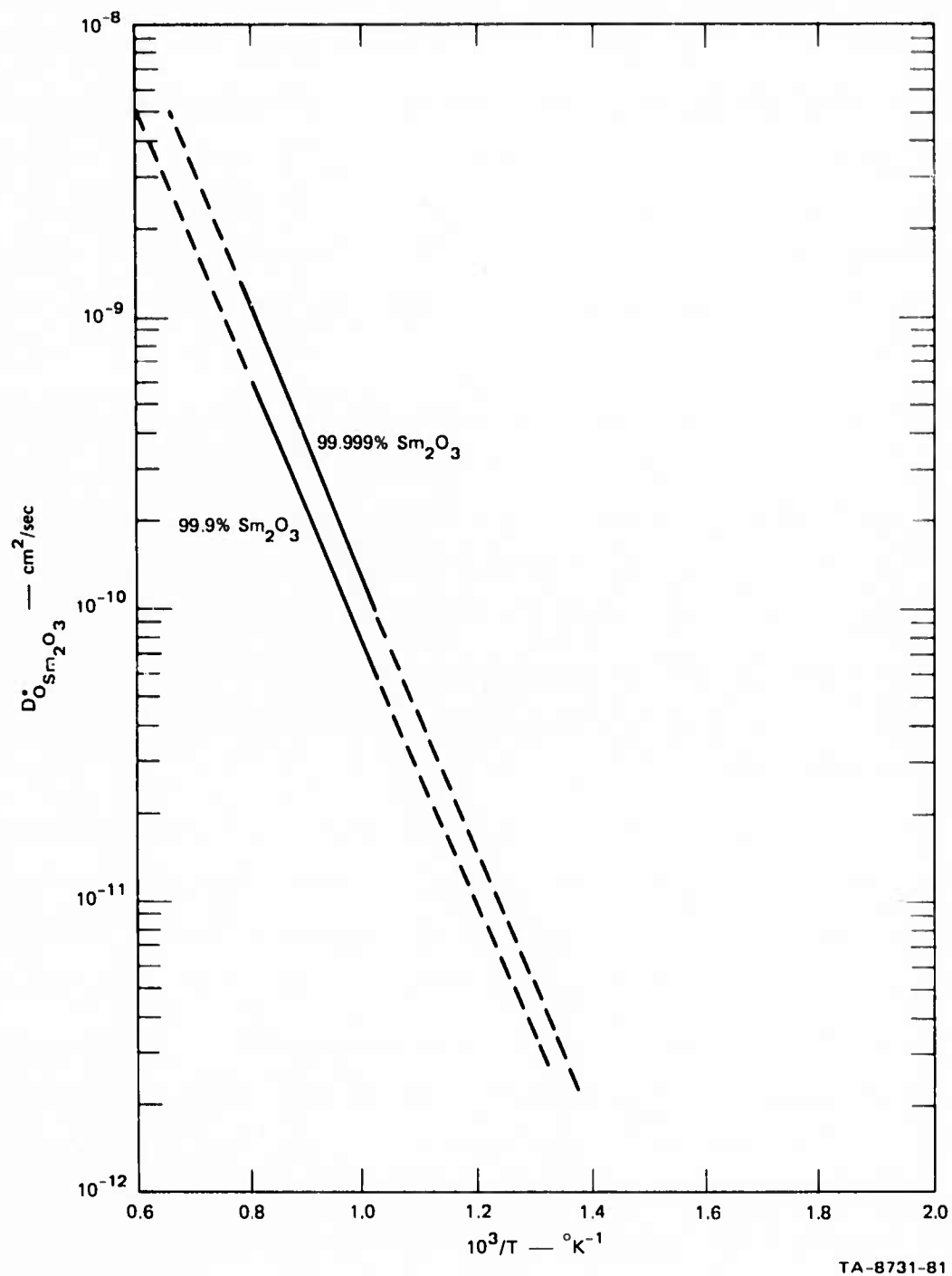


FIGURE 10 OXYGEN SELF-DIFFUSION IN B-TYPE Sm_2O_3 (AFTER STONE⁶)

1.15 g/cm³ and the actual driving force could only represent a concentration difference that is matched by an appropriate point-defect concentration difference in the oxide that would be undoubtedly much smaller than the total oxygen concentration in the oxide. It is quite clear from these calculations that if oxygen transport through the oxide is the rate-limiting step, then the diffusivity must be much faster than the diffusivity observed by Stone⁶ and by other investigators involved in the diffusion of oxygen or reoxidation of partially reduced B-type and C-type rare earth sesquioxides.

Vacuum annealing a partially oxidized sample at a temperature higher than the oxidation temperature evidently prevents further oxidation when the sample reenters oxygen. As discussed in the next section, annealing causes dissolution of the aligned fibers in the subscale and reprecipitation of larger, more equidimensional oxide particles. The samarium oxide particles remain as the dispersed phase in the subscale while β -cobalt and, additionally, $\text{Sm}_2\text{Co}_{17}$ are the matrix phases as a result of high temperature vacuum annealing.

If rapid oxygen transport through α -cobalt were rate-controlling, then continued oxidation would be expected after vacuum annealing and reexposing the specimen to oxygen at elevated temperatures. Hence, oxygen diffusion in the cobalt phase is eliminated as the rate-controlling step.

The dispersed oxide phase occupies approximately 40 percent of the subscale volume and there is scanning microscopic evidence that considerable linking (sintering) exists among the various oxide particles after vacuum annealing the subscale. Hence, if oxygen anion transport through the oxide were rate-controlling, it is expected that there would be some continued oxidation rather than passivation.

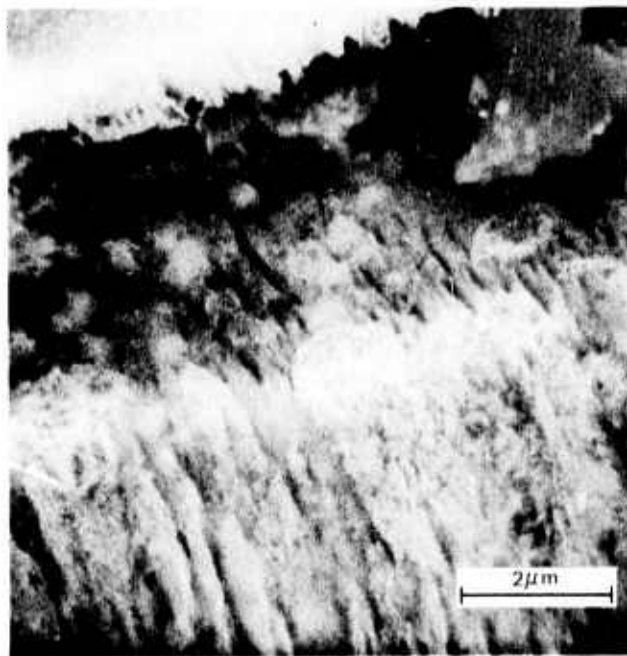
There are no consistent phase changes in either cobalt or the samarium oxides that correlate with the apparent change in activation

energy above 700°C. This supports the conclusion that bulk diffusion of oxygen in neither cobalt nor Sm_2O_3 is fast enough to account for the internal oxidation rate.

Migration of samarium outward by a vacancy exchange mechanism would cause the accumulation of internal vacancies and the precipitation of voids, which are not observed.

The rapid oxygen transport required for internal oxidation may occur along the interface between oxide fibers and β -cobalt. Because of the small dimensions of the composite microstructure of the subscale, a large amount of interface area is present. This mechanism can account for the apparent change in activation energy for the internal oxidation rate at about 700°C. The fiber size and spacing begin to increase with increasing temperature at about that temperature and the interfacial area per unit volume of oxide subscale decreases correspondingly. This effect is shown by comparing Figure 1 (1150°C) with the scanning electron micrograph shown in Figure 11 for subscale oxidation at 800°C. If it is assumed that the same transport mechanism is involved at all of the temperatures for which there are experimental data, then a reduction in the interfacial area would reduce both the number of effective conduits for oxygen transport and the apparent activation energy, even though the true activation energy for surface diffusion and the enthalpy for generating mobile species at the samarium oxide-cobalt interface remain constant.

Other experimental techniques for elucidating the mechanism of oxygen transport involved in internal oxidation of SmCo_5 have been attempted without much success. Ion microprobe analysis following oxidation of SmCo_5 with 99% O^{18} was not successful because considerable amounts of O^{16} were also observed. The source of the O^{16} is not clearly known, but evidently a considerable amount of oxygen and water vapor adsorb on the sample and is subsequently desorbed during ion microprobe analysis. This contaminating



TA-8731-91

FIGURE 11 FIBROUS SAMARIUM OXIDE WITH CRACK
IN THE SUBSCALE GROWN AT 800°C

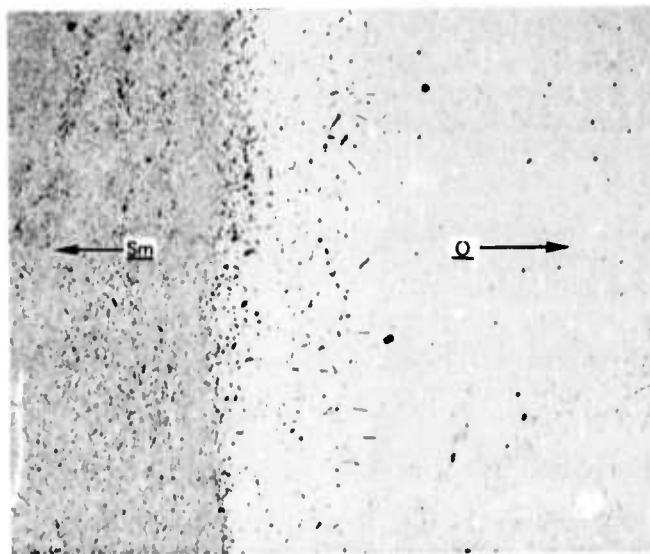
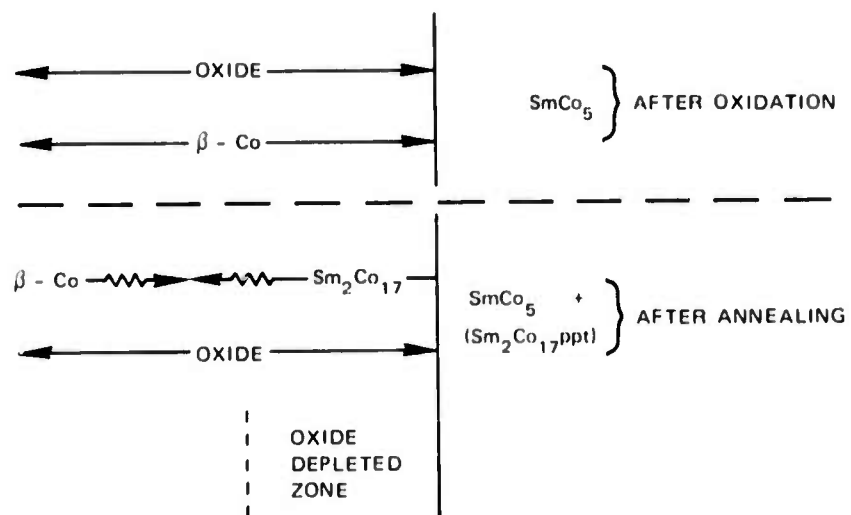
oxygen is probably adsorbed during the transfer of the sample from the O^{18} furnace chamber to the ion microprobe. Adsorbed oxygen and water vapor may continuously migrate to the ion impact area by surface diffusion and then be discharged and picked up by the ion detector. Although moderately high levels of O^{18} could also be detected with the O^{16} contamination, it was not possible to do marker experiments unambiguously, using O^{18} and subsequently detect the location of the O^{18} in the subscale.

Auger spectroscopy was also employed to investigate the oxide films formed by low temperature oxidation. These experiments also indicate that a considerable amount of adsorbed species, some of which contain oxygen, are migrating to the surface and affecting the results. In both ion probe analyses and Auger analysis, the oxygen concentration profile obtained from continued sputtering appears to extend deeper into the specimen than is known to be true from kinetic and metallographic data.

III VACUUM ANNEALING PARTIALLY OXIDIZED SmCo_5 AT SINTERING TEMPERATURES

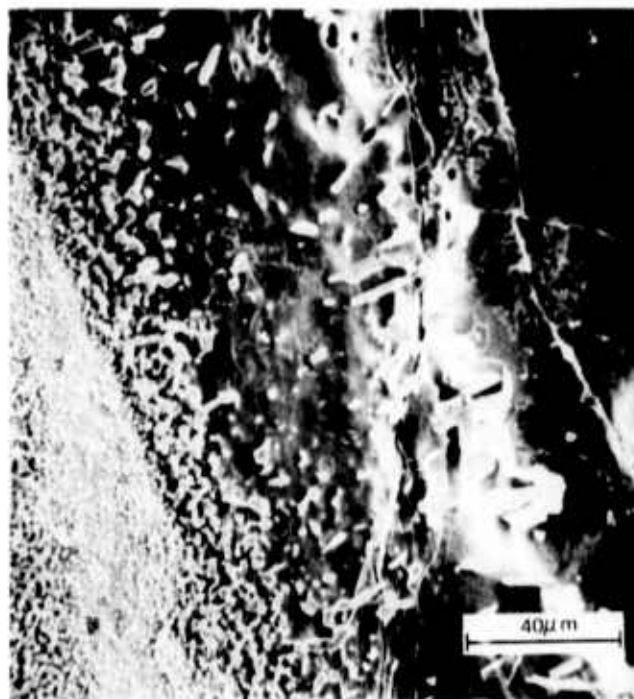
An example of the result of high temperature annealing in the absence of oxygen after partial internal oxidation of SmCo_5 is shown in Figure 12. This particular specimen was oxidized 45 minutes in air at 800°C , and was subsequently annealed 16 hours at 1125°C . A scanning electron micrograph of the same section is shown in Figure 13. The original subscale prior to vacuum annealing penetrated to the farthest extent of the large oxide particles shown in Figure 12 and had the fibrous microstructure shown in Figure 11. As a result of vacuum annealing, the fine samarium oxide fibers have recrystallized into large, roughly equidimensional particles. The subscale contains a conjugate zone partially depleted in samarium oxide adjacent to the original SmCo_5 core. The few oxide particles in the oxide depleted zone are considerably larger than the oxide particles in the undepleted part of the subscale. A higher magnification view of the reprecipitated oxide particles is shown in Figure 14.

The oxide particles and alloy phases have been identified by electron beam microprobe analyses. The matrix of the depleted region consists of $\text{Sm}_2\text{Co}_{17}$. This phase results because samarium is transported from the SmCo_5 core into the subscale region where it reacts with cobalt. The SmCo_5 core is transformed from a single phase region into an SmCo_5 matrix containing $\text{Sm}_2\text{Co}_{17}$ precipitates as a result of samarium depletion from the core. The solid state diffusion and precipitation reactions are:



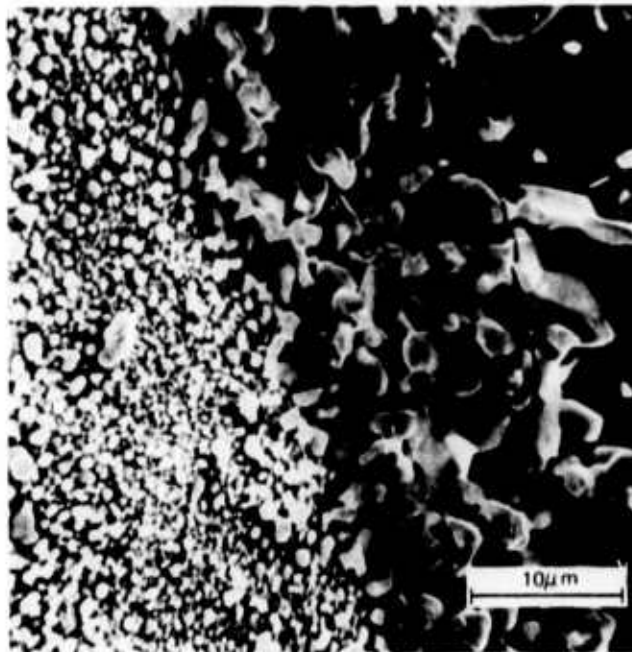
TA-8731-85R

FIGURE 12 OXIDE DEPLETION ZONE RESULTING FROM INTERNAL OXIDATION OF SmCo_5 FOLLOWED BY VACUUM ANNEALING, 125X



SA-8731-92

FIGURE 13 OXIDE DEPLETION ZONE AT HIGHER MAGNIFICATION (SEM)

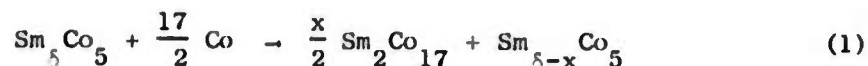


SA-8731-93

FIGURE 14 BOUNDARY OF THE OXIDE DEPLETED
ZONE (RIGHT SIDE) WITHIN THE SUBSCALE

(1) At vacuum annealing temperature, diffusion reaction:

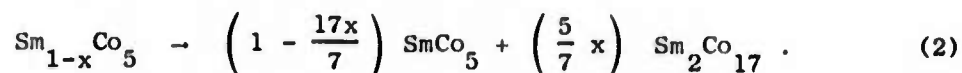
core + subscale matrix \rightarrow subscale matrix + core



where $\delta \sim 1$.

(2) During quenching, precipitation:

if $\delta = 1$, then



While samarium migrates out of the core, oxygen dissolves and migrates into the core, causing the reduction in population of oxide particles in the depleted zone. This phenomenon is a direct result of the solubility of oxygen in SmCo_5 at the higher vacuum annealing temperature, 1125°C . Although the vacuum annealing time in this case was 16 hours, identical results have been obtained with a 30-minute vacuum anneal, which is identical to our standard magnet sintering time and temperature.

The scanning electron micrograph shown in Figure 15 shows essentially all of the features of this system. The original boundary separating the subscale from the SmCo_5 core is shown. Below this boundary is the region containing a $\text{Sm}_2\text{Co}_{17}$ matrix and large samarium oxide particles. A two-phase alloy region consisting of a SmCo_5 matrix and $\text{Sm}_2\text{Co}_{17}$ precipitates exists above the boundary. A relic of the original fibrous subscale is also shown in this unusual SEM micrograph. A small samarium oxide particle is also shown in the core region above the boundary line. This particle is produced by oxygen dissolved in SmCo_5 and subsequently precipitated on cooling.



SA 8731-94

FIGURE 15 BOUNDARY BETWEEN THE OXIDE
DEPLETED ZONE AND THE SmCo_5
CORE

IV OXYGEN SOLUBILITY DURING SINTERING AND SUBSEQUENT OXIDE PRE- CIPITATION IN SmCo_5

Attention is now turned to the problem of oxide dissolution in SmCo_5 at sintering temperatures and the subsequent redistribution of the oxide on cooling.

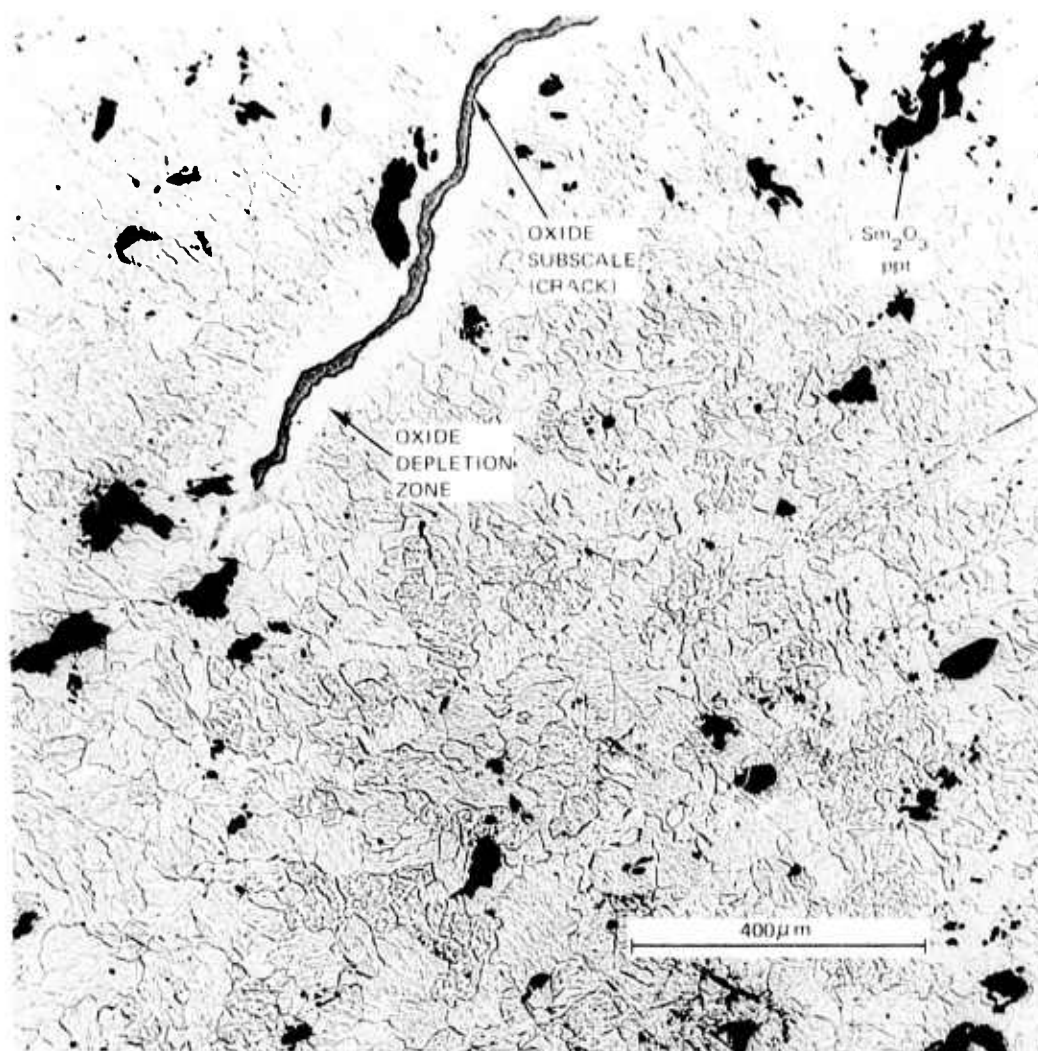
The experimental procedure used in this study has been to introduce considerable amounts of oxygen deliberately into the SmCo_5 system using small polycrystalline cast pieces by first partially oxidizing the relatively oxygen-free alloy. Because of their large grain size and absence of porosity, the cast alloys are easier to examine metallographically by SEM and by EBM methods than sintered magnets. An oxidation temperature of 800°C was chosen because it is substantially below the sintering temperature, and the homogeneity range in SmCo_5 is believed to be extremely narrow at that temperature. Furthermore, it has been shown that aging sintered SmCo_5 magnets at about this temperature (usually 900°C) can often be beneficial to the magnetic properties. In particular, an increase in magnetic coercivity is often obtained.¹⁰ After oxidation, the specimens were vacuum annealed at 1120 to 1125°C for 30 minutes. We were initially concerned about obtaining chemical equilibrium through the entire ingot, which is typically 0.5 cm on edge, and therefore very long annealing times were used. Subsequently, we found that the standard sintering time, 30 minutes, is sufficient to provide a macroscopically homogeneous distribution of oxygen in the SmCo_5 core of such large alloy pieces. The initial alloy had the stoichiometric SmCo_5 composition, i.e., there was essentially no depletion of samarium.

The results will be described for specimens after vacuum annealing at sintering conditions and also after a third heat treatment, i.e.,

aging at 800°C for 45 minutes. For convenience we will refer to the two types of specimens as "quenched" and "aged." Quenched specimens are produced by quickly removing the specimen from the furnace, but cooling occurs in vacuo so that "normalized" would be a more appropriate classical metallurgical term.

The amount of oxygen transferred from the oxide subseale into the SmCo_5 was crudely estimated by measuring the thickness and the area of the depletion zone. This estimate is not very accurate because not all of the oxide in the depletion zone is dissolved. From inspection of Figure 13 and similar photographs it was estimated that 75 percent of the oxide in the depleted zone was dissolved. The calculation indicated that the solubility of oxygen in SmCo_5 at 1125°C in excess of the solubility at 800°C is ~ 0.35 wt%. It is impossible to put error limits on this estimate.

Next, the oxide content within the core of an aged specimen was calculated metallographically. Large oxide particles are produced as a result of the aging treatment and these oxide particles appear black under reflected light; see Figure 16. Consequently, a Quantimet image analysis was performed on several sections and the area percent of oxide was determined. The average area of oxide particles and the limits were determined to be $2.6 \pm 0.4\%$. The area percent is equal to the volume percent for randomly distributed equidimensional particles in a dilute suspension. Hence, from the volume of oxide in the core obtained after aging, the excess solubility of oxygen at the sintering temperature was determined. This calculation involves the implicit assumption that all of the soluble oxygen in excess of the 800°C solubility limit was precipitated as measurably large oxide particles during the 45-minute aging treatment at 800°C. The precipitation and growth of extremely large oxide particles during this period, as shown in Figure 16, indicates that



SA 8731 95

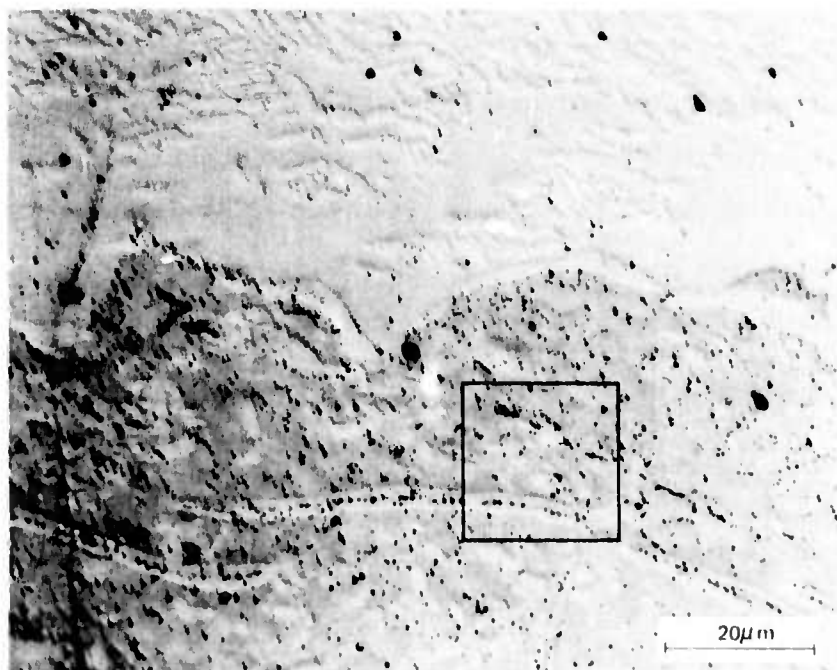
FIGURE 16 OXIDE PRECIPITATES IN THE SmCo_5 GRAINS AFTER OXYGEN SATURATION AT 1125°C AND AGING AT 800°C

this assumption is valid. The metallographic determination of the excess solubility at 1125°C is $0.35 \pm 0.05 \text{ wt\%}$ ($3500 \pm 500 \text{ ppm}$).

Although the oxide particles observed in the aged specimens were sometimes larger than 100 micrometers, particles in the quenched specimens are generally smaller than one micrometer. Any exceptions can usually be traced back to larger oxide inclusions that were present after melting. The oxide particle population is greater in the quenched specimens than in the aged specimens, as shown by contrasting the quenched and aged specimens illustrated in Figure 17. Again, the specimens were castings subsequently oxidized and annealed at 1125° before quenching. These micrographs were obtained from surfaces polished using cerium oxide but not etched. The background also shows a faint relief of larger $\text{Sm}_2\text{Co}_{17}$ precipitates, which will be discussed in the next section. However, a large amount of oxygen known to be present in the specimen is not accounted for in the low particle population regions of the quenched specimen, which is most of the specimen. This oxygen may occur as small particles below the resolution limit, as coherent oxygen-rich zones, or as a supersaturated solute. The aging process collects the smaller oxide particles into a few large particles by a solution-reprecipitation process.

The quenched specimen micrograph of Figure 17 shows a region of low oxide particle population in the upper part of the figure and a region of high particle population in the lower half of the figure. High particle population regions were less common than low particle population regions in the specimens examined. The boxed area in Figure 17 was picked at random within the high particle population region. The average oxide particle size is 0.4 micrometer and the volume fraction of oxide, V_f , was determined from

$$V_f = \frac{\pi}{6} N_s \bar{d}_p^3 \quad (3)$$



(a) QUENCHED FROM 1125 °C



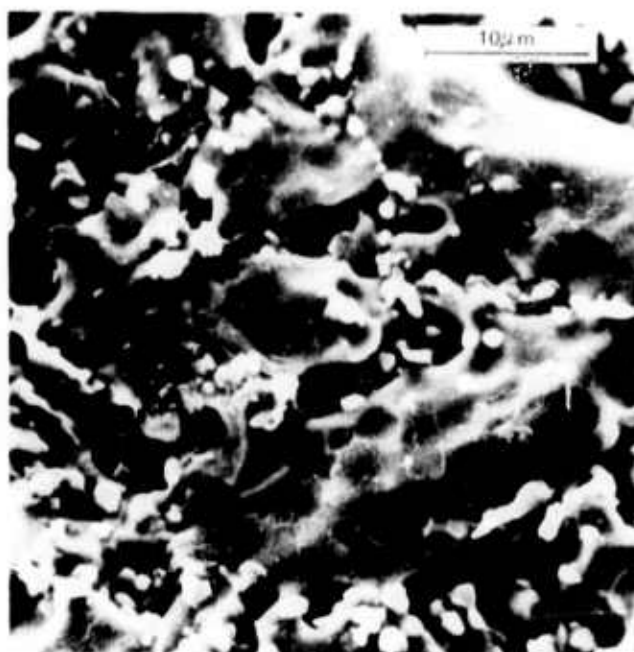
(b) QUENCHED AND AGED AT 800 °C

SA-8731-96

FIGURE 17 QUENCHED AND AGED SmCo_5 GRAINS

where N_s is the particle population per unit area, and \bar{d}_p is the mean particle diameter. The particle population in the boxed area was 3.0×10^7 particles/cm². The resulting volume fraction was 0.025 (2.5%), which is very similar to the volume fraction (2.6%) in aged specimens. Hence, in the high population regions, most of the dissolved oxygen has precipitated as submicron but visible particles.

The appearance of small oxide inclusions within the primary SmCo₅ grains of both experimental and commercial sintered magnets has also been observed. These magnets did not receive an aging treatment. Small oxide particles generally appear within the SmCo₅ grains rather than at grain boundaries. Fracture surfaces have also been examined with a scanning electron micrograph and oxide particles are rarely observed until the specimen is etched. Numerous oxide particles which were present in the SmCo₅ grains are uncovered by etching. Exposed oxide particles in an etched sintered magnet are shown in Figure 18. The dark areas in this scanning electron micrograph are pores.



SA 8731 97

FIGURE 18 SAMARIUM OXIDE PARTICLES IN A
SINTERED SmCo_5 MAGNET UNCOVERED
BY ETCHING

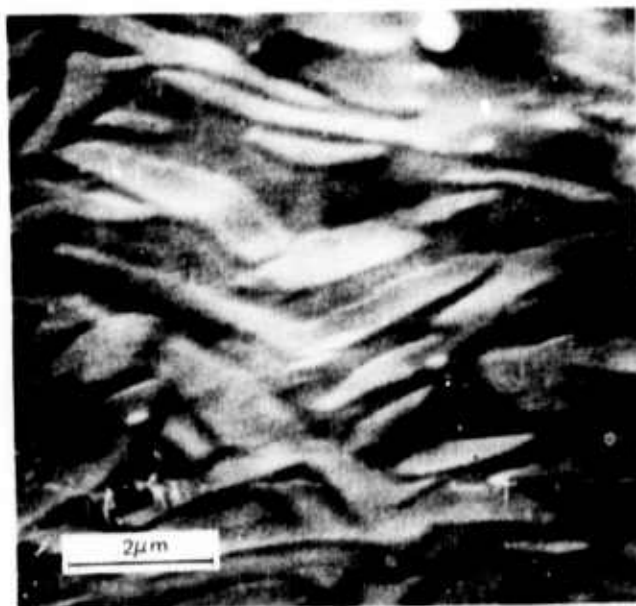
V PRECIPITATION OF $\text{Sm}_2\text{Co}_{17}$ IN SmCo_5

A study was made of the precipitation of the $\text{Sm}_2\text{Co}_{17}$ phase in samarium-depleted SmCo_5 using cast pieces. There are two stages of $\text{Sm}_2\text{Co}_{17}$ precipitation in SmCo_5 as a result of partial oxidation followed by sintering or vacuum annealing. The primary stage results from samarium depletion caused by reaction between the SmCo_5 core and α -cobalt in the subscale. This reaction occurs during the sinter-annealing process described by Equation (1). As a single phase alloy is quenched from 1125°C , precipitates of $\text{Sm}_2\text{Co}_{17}$ occur within the SmCo_5 grain as described by Equation (2). These precipitates are one micrometer wide and a few micrometers long. They often occur in clusters as shown by the scanning electron micrograph in Figure 19.

One small samarium oxide precipitate also appears in this micrograph. The average SmCo_5 grain size, which is controlled by solidification, was about 80 micrometers in our test specimens. There was no tendency for $\text{Sm}_2\text{Co}_{17}$ to precipitate at the SmCo_5 grain boundaries during the primary stage of $\text{Sm}_2\text{Co}_{17}$ precipitation after vacuum annealing at sintering temperatures. However, cobalt-rich specimens quenched from the melt exhibit $\text{Sm}_2\text{Co}_{17}$ at boundaries of SmCo_5 grains.

It should be emphasized that primary precipitation of $\text{Sm}_2\text{Co}_{17}$ within the SmCo_5 grains occurs whenever excess cobalt is exsolved from a samarium-depleted SmCo_5 phase during cooling, whether the cause of samarium depletion is oxidation or not.

Primary $\text{Sm}_2\text{Co}_{17}$ precipitation is evidently complete on quenching in vacuo. A series of aging tests for various times at 800°C using pieces from a samarium-depleted double melted ingot (not oxidized) showed no increase in the amount of $\text{Sm}_2\text{Co}_{17}$ or any apparent rearrangement of $\text{Sm}_2\text{Co}_{17}$ as a result of aging.



SA 8731-98

FIGURE 19 SCANNING ELECTROMICROGRAPH OF
 $\text{Sm}_2\text{Co}_{17}$ PRECIPITATES IN SmCo_5

The second stage of $\text{Sm}_2\text{Co}_{17}$ precipitation is caused by rejection of oxygen dissolved in SmCo_5 and formation of Sm_2O_3 . As already mentioned, this does not occur to any appreciable extent during quenching, but it does occur with aging. During the aging process, both samarium and oxygen are collected at the large oxide particles and must diffuse over distances relatively large when compared with the primary SmCo_5 grain size. Further depletion of samarium from primary grains and rejection of additional $\text{Sm}_2\text{Co}_{17}$ results. Micrographs indicate that this secondary precipitation of $\text{Sm}_2\text{Co}_{17}$ occurs at the SmCo_5 grain boundaries rather than within the grains. This is particularly evident in the aged specimen micrograph of Figure 17.

The precipitation of large Sm_2O_3 particles is probably controlled by rapid grain boundary diffusion of samarium. This process causes bulk depletion of samarium from the region adjacent to SmCo_5 grain boundaries and precipitation of $\text{Sm}_2\text{Co}_{17}$ in the samarium-depleted zone, which is about 2 micrometers wide. This model is consistent with the rate of solid state sintering of SmCo_5 , a process that is also controlled by grain boundary diffusion.

Similar behavior has been observed in sintered magnets. However, when the primary SmCo_5 grain size is small, ~ 5 micrometers, the $\text{Sm}_2\text{Co}_{17}$ precipitates are no smaller than observed in cast pieces, and, hence, nearly as large as the primary grains.

The precipitation of fine $\text{Sm}_2\text{Co}_{17}$ particles in samarium-depleted alloys contrasts sharply with the Sm_2Co_7 phase in samarium-rich alloys. In the latter case the primary SmCo_5 grains are clean and Sm_2Co_7 occurs as separate grains outside the SmCo_5 primary grains.

VI DISCUSSION OF Sm_2O_3 AND $\text{Sm}_2\text{Co}_{17}$ INCLUSIONS AND INTRINSIC COERCIVITY IN SmCo_5 SINTERED MAGNETS

A. Summary of Inclusions

It is now quite clear that internal surfaces can occur in primary SmCo_5 grains of sintered magnets from precipitation of second phase inclusions: $\text{Sm}_2\text{Co}_{17}$ and Sm_2O_3 . Although the oxygen solubility determinations for cast SmCo_5 are not very precise, it is certain that large amounts of oxygen can dissolve in SmCo_5 at sintering temperatures. For careful processing operations, where oxygen contamination is kept below 3500 ppm, all of the oxygen will be dissolved in SmCo_5 during sintering. The normal quenching of sintered magnets is expected to leave approximately one-micrometer oxide particles within the SmCo_5 grains, which has been verified in sintered magnets. Much of the oxygen in quenched SmCo_5 is unaccounted for and may be present as supersaturated oxygen, coherent oxygen-rich zones, and unresolvable oxide inclusions. Selective oxidation of the alloy also affects the formation of $\text{Sm}_2\text{Co}_{17}$ by depleting samarium and shifting the composition, and this occurs in two sequential stages.

Although oxidation cannot be entirely prevented, primary and secondary formation of $\text{Sm}_2\text{Co}_{17}$ precipitates can be prevented by having excess samarium present in the powder compact to replace the samarium depleted from SmCo_5 grains. Oxide precipitates can be removed from the primary magnet grains by an aging treatment that tends to collect the oxygen in a few large oxide grains. Optimum aging conditions need to be determined.

B. Inclusions and Intrinsic Coercivity

This section begins with a brief review of coercivity models for high

magnetocrystalline anisotropy magnet materials. For a detailed review, see Livingston.¹¹ The highest published room temperature intrinsic coercivity in sintered SmCo_5 magnets is $H_{c1} = 43 \text{ kOe}$.¹² A sintered SmCo_5 magnet with a room temperature intrinsic coercivity of 43 kOe has also been produced and measured at SRI.³ This is only about 15% of the theoretical coercivity, $2 K/M_s$, where K is the magnetocrystalline anisotropy and M_s is the saturation magnetization. Furthermore, sintered SmCo_5 magnets usually have much lower coercivities and SmCo_5 powders and samarium-depleted sintered magnets usually have intrinsic coercivities well below 20 kOe.

Because of the high magnetocrystalline anisotropy, coherent rotation of domains and curling cannot occur at the comparatively low fields at which magnetic reversal actually occurs.

Magnetic domain nucleation and domain-wall pinning are factors that may control coercivity. Inclusions and possibly other defects such as stacking faults and coherent zones of second phase material are expected to impede domain-wall movement and increase coercivity. However, these same defects can act as nucleation sites for new domains and decrease coercivity. The experimental results show conclusively that processing operations that lead to Sm_2O_3 and $\text{Sm}_2\text{Co}_{17}$ inclusions within SmCo_5 grain boundaries always lower coercivity and conversely processing operations that decrease these inclusions raise coercivity. Hence, nucleation of domains rather than domain-wall pinning evidently controls coercivity.

Additional arguments against a domain-wall pinning model can be made based on other experimental information. Sintered rare earth cobalt magnets are made by aligning the powder (easy axis crystallographic parallel orientation). During sintering the crystallographic orientation is maintained but the specimen is thermally demagnetized. If domain-wall motion controlled the coercivity, then magnetization of the sintered specimen should require a high field similar to H_{c1} . The

experimental evidence is that magnetization nearly equal to M_s can be obtained in a thermally demagnetized specimen at fields much lower than H_{c1} .

Domains have been observed in a large number of SmCo_5 grains in which $\text{Sm}_2\text{Co}_{17}$ inclusions have been introduced by samarium depletion. Bending of domain walls around these inclusions¹³ or termination of domains at internal inclusions has never been observed in this laboratory. In all cases the domain walls seem to be oblivious to the presence of the cobalt-rich inclusions. A typical micrograph of domains in SmCo_5 grains with $\text{Sm}_2\text{Co}_{17}$ precipitates is shown in Figure 20. A small domain apparently growing out of the grain boundary which is a region of $\text{Sm}_2\text{Co}_{17}$ can be seen in this micrograph.

Small oxide particles, ≤ 1 micrometer, such as those shown in the quenched specimen of Figure 17 also do not appear to have a preferred locus coincidental with domain walls and, therefore, are evidently not pinning domain walls. However, we do not have much evidence on this yet.

An inclusion domain-nucleation model can explain most if not all of the confirmed phenomenological relations between samarium-cobalt magnet processing and the resulting intrinsic coercivity. By confirmed phenomenological relationships we mean behavior that has been observed in more than one laboratory or is generally accepted. An example is the observed drastic decrease in coercivity if excess samarium is not present during sintering. According to this model, both Sm_2O_3 and $\text{Sm}_2\text{Co}_{17}$ inclusions, which may be submicroscopic, can heterogeneously nucleate new domains. Magnetic coercivity of a grain and of a sintered aggregate will decrease as the population of small inclusions increases.

Rather than present a lengthy discussion of these phenomena and their possible association with inclusions, we have chosen to list effects with postulated causes in Table 1.



SA 8731 99

FIGURE 20 MAGNETIC DOMAINS PASSING THROUGH $\text{Sm}_2\text{Co}_{17}$ PRECIPITATES
WITHIN SmCo_5 GRAINS

Table 1

SOME EFFECTS INVOLVING MAGNETIC COERCIVITY IN SmCo_5 AND THEIR POSSIBLE CAUSES

Effects	Possible Causes
Excess Sm is required to obtain high H_{ci} in sintered magnets	Excess Sm replenishes that depleted from SmCo_5 by oxidation and prevents exsolving of $\text{Sm}_2\text{Co}_{17}$ precipitates.
Aging at 800 to 1000°C increases H_{ci} in sintered magnets containing excess Sm	Aging scavenges Sm_2O_3 in large grains and removes fine oxide inclusions from the primary SmCo_5 grains.
Low temperature aging and very short time high temperature annealing in plasma lower H_{ci} in single particles	Surface oxide dissolves in SmCo_5 and reprecipitates as submicron oxide inclusions. Insufficient time or temperature is available to scavenge Sm_2O_3 into large grains. Also, there is no source of Sm to replenish that lost by oxidation, hence $\text{Sm}_2\text{Co}_{17}$ is precipitated.
Excessive sintering temperature lowers H_{ci}	Oxygen solubility increases with temperature and causes more inclusions of oxide and $\text{Sm}_2\text{Co}_{17}$ on cooling.
Etching increases H_{ci} in single particles	Etching removes the oxide subscale which is a source of domain nucleation at particle surfaces.
Decrease in H_{ci} with long time aging at room temperature in single particles is accelerated in the presence of oxygen	Selective surface oxidation of Sm occurs to form the oxide subscale. This would not happen if the system were truly free of any oxygen.
Overgrinding decreases H_{ci} in single particles	Surface oxidation increases per unit volume of material during grinding or following grinding and exposure to air. Grinding in the presence of small amounts of oxygen is much more deleterious than grinding in lesser amounts of oxygen.
Grinding in liquid nitrogen improves H_{ci} of particles compared with room temperature grinding	The oxidation kinetics are reduced at the lower temperature.
The outer shell ($\sim 200 \mu\text{m}$) of sintered magnet bodies has low coercivity	Oxidation or loss of Sm by evaporation causes inclusions to form--this has been observed metallographically.

VII SINTERING

A. Introduction

Benz and Martin studied the mechanism of sintering of rare-earth cobalt alloys,¹⁴ and postulated that the sintering kinetics are controlled by the diffusion of samarium atoms in grain boundaries via a samarium atom-cobalt vacancy cluster exchange mechanism. This conclusion was based on an observed one-third time dependence of volume shrinkage calculated from end point densities of samples that initially contained a liquid phase, and on a comparison of the total volume shrinkage or density with the alloy composition. Benz and Martin further noted that a correlation existed between the conditions that produced rapid shrinkage and the conditions that yielded high intrinsic coercivity, and since this correlation has important processing implications, it was decided to follow the solid phase stage of sintering of SmCo_5 under conditions in which kinetic models could be applied thus allowing a study of the effect of changes in stoichiometry on the kinetics of sintering.

The sintering kinetics of solids have been studied extensively beginning with Kuczynski¹⁵ and then followed by Kingery and Berg,¹⁶ Coble,¹⁷ and Johnson and Cutler.¹⁸ Refinements in the assumptions relating the mathematical models to the physical model have been made primarily by Johnson.¹⁹ From these studies the general equation for solid state sintering is given as

$$\frac{\Delta L}{L_o} = \left(\frac{K\gamma\Omega D}{kTr^n} \right)^m t^m \quad (4)$$

where

$\Delta L/L_0$ = the fractional shrinkage

γ = the surface free energy

Ω = the volume transported per atom of the rate-controlling species

D = the self-diffusion coefficient of the rate-controlling species

k = Boltzmann's constant

T = absolute temperature

r = the particle or powder radius

K, n, m = constants that depend on the sintering mechanism.

Table 2 lists the values of the constants versus the sintering mechanism.

Table 2

SINTERING CONSTANTS FOR EQUATION (4)

Sintering Mechanism	K	n	m	Reference
Volume Diffusion	5.34	3	0.49	5
	$20/\sqrt{2}$	3	0.40	2
	2	3	0.50	3
Grain Boundary Diffusion	2.14b	4	0.33	5
	3b	4	0.33	3

The symbol b in Table 2 is the grain boundary width. The constant m is usually determined by plotting the logarithm of fractional shrinkage versus the logarithm of time, and a sintering mechanism is deduced based on the value of m. This method of determining the sintering mechanism

is not precise unless time and length corrections are applied, because n varies with small errors in time and shrinkage. The errors result from the inability to heat the sample instantaneously to the sintering temperature. Lay and Carter²⁰ have outlined a relatively easy method of correcting the time and length that involves calculating L_0 from thermal expansion data and extrapolating a length versus time plot to intersect the calculated L_0 value, thus determining the effective initial time.

Johnson²¹ later pointed out that the method of Lay and Carter is strictly valid only if an array of identically sized spheres are used in the study, and if it is known that all of the mass transport is due to a single mechanism.

The sintering studies described in this report are incomplete in that a complete range of stoichiometries has not been investigated and the validity of assuming a single transport mechanism has not been tested.

B. Experimental Procedure

Samarium-cobalt alloy powders were made for this study by arc melting the elements. Slight changes in the alloy compositions were obtained by adjusting the samarium/cobalt ratio used in the arc melting. The arc-melted alloys were annealed in an oxygen-gettered argon atmosphere at 1110°C for four hours, and were then individually ground in an alumina ball mill for three hours using sodium-gettered hexane as the milling fluid. The final alloy compositions were determined from EDTA titration data,²² and the compositions were adjusted for loss of samarium due to the formation of Sm_2O_3 . The oxygen concentrations in the alloys were determined by neutron activation analysis and by vacuum fusion analysis (courtesy of General Electric Company). The oxygen content in solid solution was assumed to be zero.

Disk-shaped specimens 1.0 inch in diameter by 0.13 inch thick, were fabricated by die pressing at 30,000 psi in the absence of a magnetic field. The specimens were placed on a molybdenum support in a furnace employing a graphite resistance heater surrounded by oxygen-gettered argon. The change in sample diameter was recorded by time-lapse photography as functions of time and temperature, and the data were read from the films by means of a Telereadex film analyzer.

Sample length corrections were made following the method of Lay and Carter²⁰ using the thermal expansion data presented in Figure 21, which were obtained by using a commercial dilatometer modified so that a static argon atmosphere could be used to surround the sample to prevent oxidation.

Heating the sintering samples from room temperature to the sintering temperature required approximately 90 seconds. Shrinkage below approximately 1100°C is almost negligible and the time required to reach 1165°C from 1100°C was approximately 5 seconds. Calculated L_o values (initial sample diameter) corresponded exactly with the experimentally measured L_o values at 1100°C. At 1120°C a small correction in L_o was required and these corrections increased in magnitude as the sintering temperature was raised to 1165°C, indicating that shrinkage was occurring as the sample was heated from 1100 to 1165°C. The corrections ranged from 0.0% at 1100°C to less than 2.0% at 1165°C.

C. Results and Discussion

Shrinkage data were obtained for four different alloy comparisons, and these data are shown in Figures 22, 23, and 24. The value of m (see Eq. 4) as determined by a least-squares analysis ranged between 0.24 and 0.37. The correlation coefficient except for one isotherm was above 0.93. Thus the shrinkage data approximate a slope of $m = 0.33$ and indicate that the shrinkage is controlled by grain boundary diffusion.

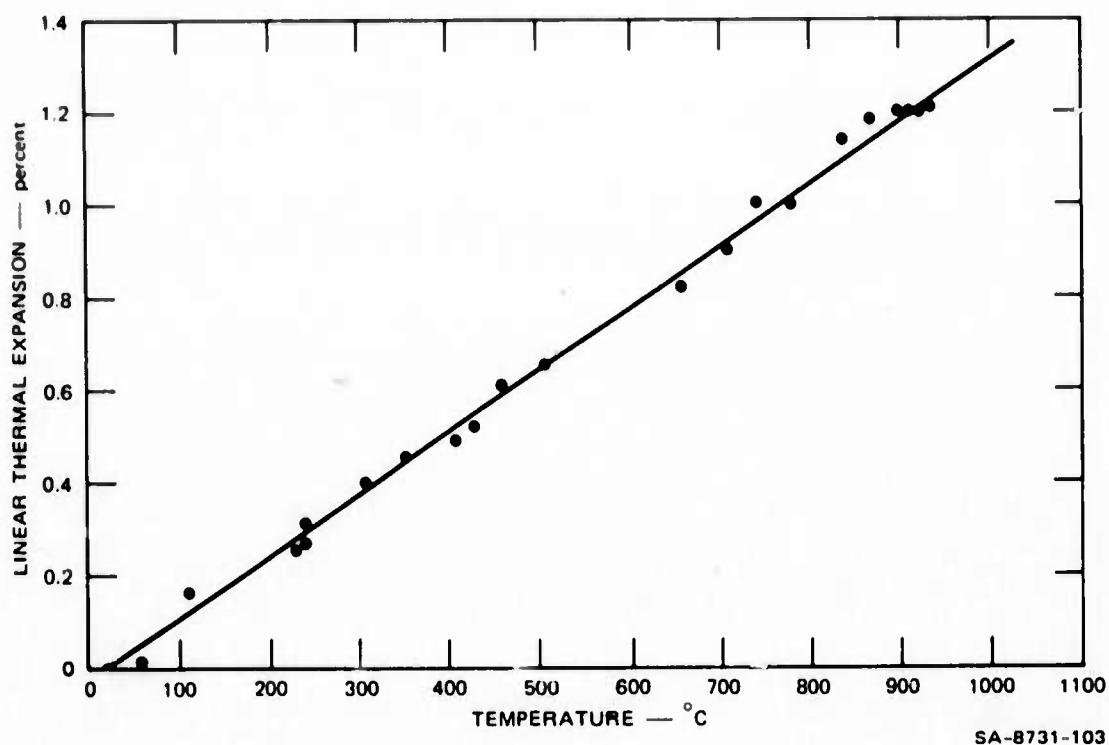


FIGURE 21 LINEAR THERMAL EXPANSION OF POLYCRYSTALLINE RANDOMLY ORIENTED SmCo_5

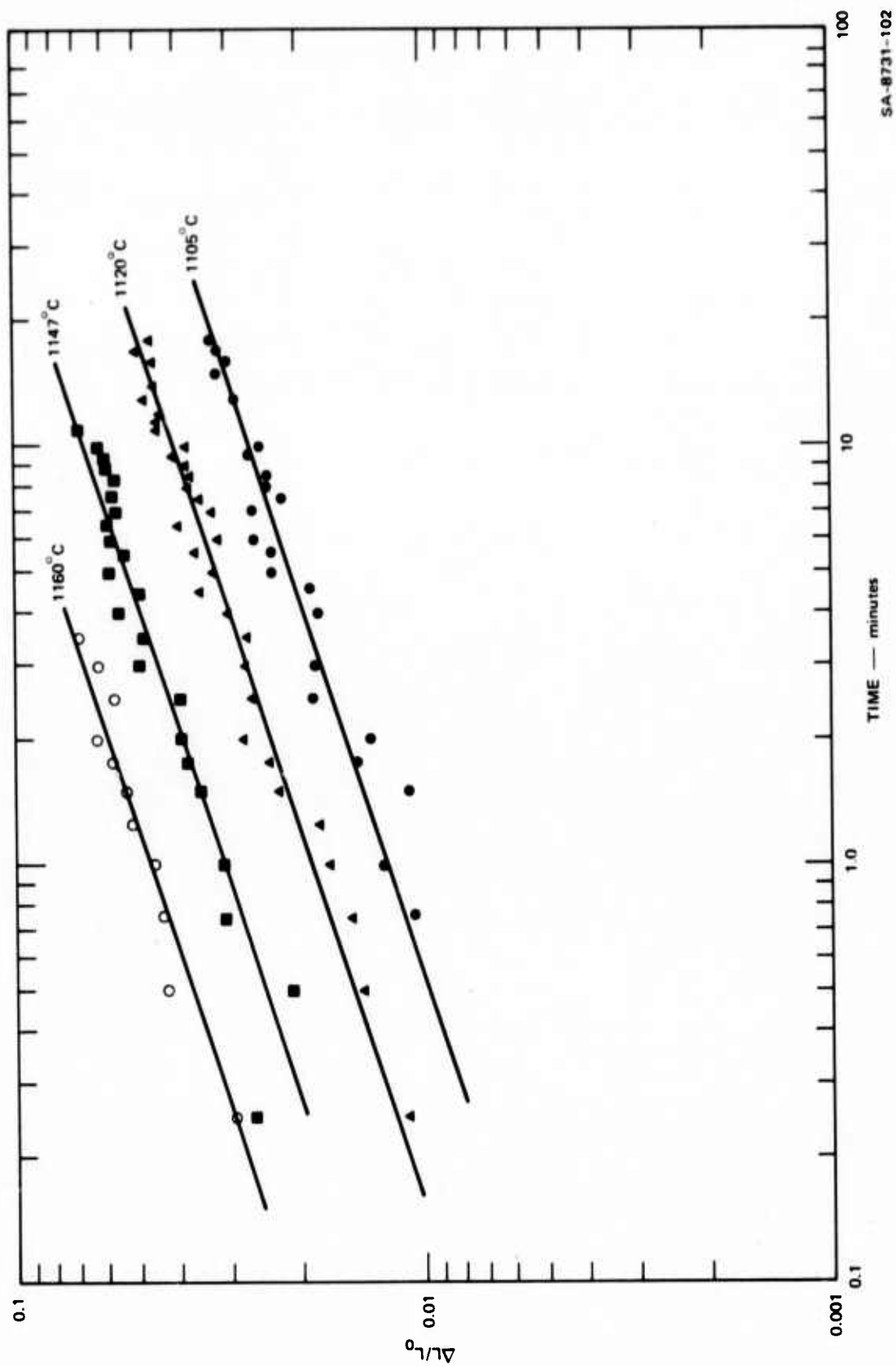


FIGURE 22 SAMARIUM-COBALT SHRINKAGE ISOTHERMS FOR AN ALLOY CONTAINING 27.7 wt% Sm

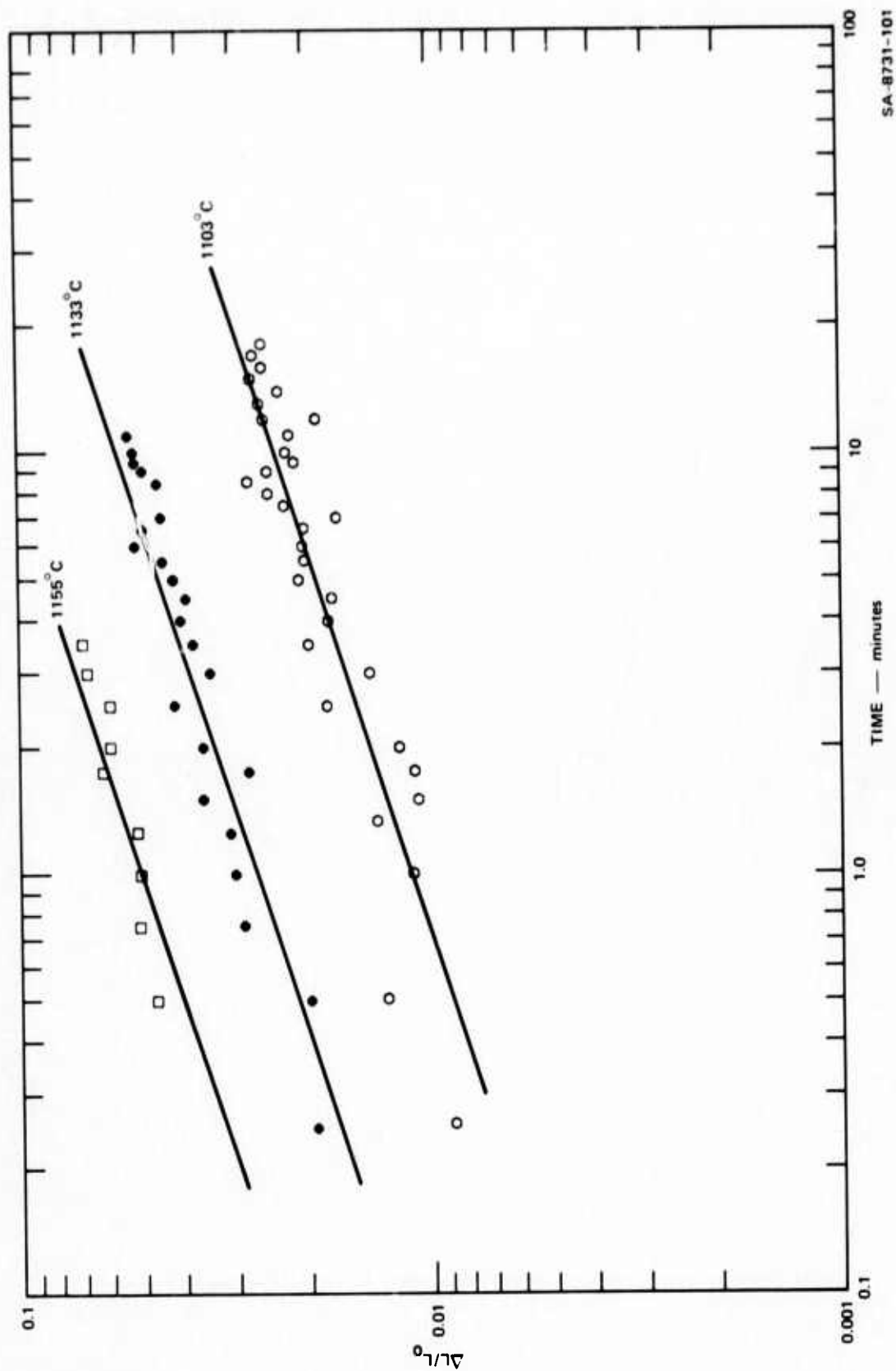


FIGURE 23 SAMARIUM-COBALT SHRINKAGE ISOTHERMS FOR AN ALLOY CONTAINING 31.35 wt% Sm

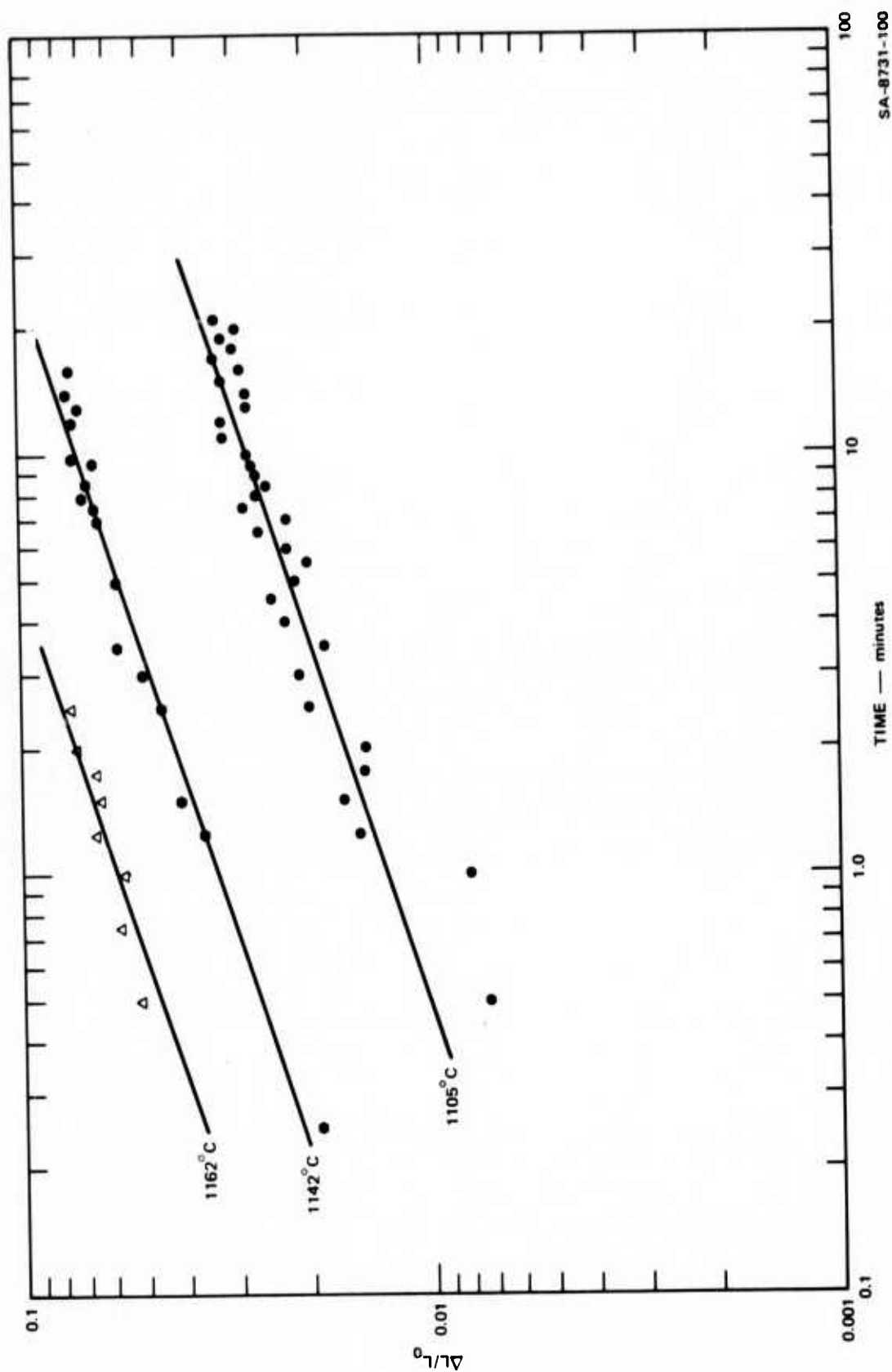


FIGURE 24 SAMARIUM-COBALT SHRINKAGE ISOTHERMS FOR ALLOYS CONTAINING 33.0 AND 33.33 wt% Sm

The data presented in Figures 22, 23, and 24 were force fitted to lines drawn with slopes equal to 0.33, and the data near 1100°C exhibit considerable scatter due to the small amounts of shrinkage involved. The rate of shrinkage can be calculated from the intercept values for each isotherm, and the rate of shrinkage is shown plotted versus reciprocal temperatures in Figure 25. All four alloy compositions exhibit identical rates of shrinkage within experimental error and this result is in conflict with the results of Benz and Martin.¹⁴

SmCo₅ alloy compositions are very sensitive to the oxygen impurity concentration. Therefore the oxygen content of the alloys used in this study were determined by both neutron activation analysis and by vacuum fusion analysis. These methods of analysis for oxygen in SmCo₅ give conflicting results with the vacuum fusion method always exhibiting the higher value. The results of the oxygen analysis are listed in Table 3. Because of the discrepancies shown in Table 3, very brief descriptions of the two oxygen analysis techniques are given below.

The neutron activation analysis was conducted by Gulf Radiation Technology Company. Each sample was irradiated for 10 seconds in a 14-MeV neutron flux of approximately 10^8 neutrons/cm²-sec. An oxygen standard was irradiated with each sample and the induced activity of N¹⁶ was counted on a single channel pulse-height analyzer using a pair of 5 x 5-inch NaI(Tl) scintillation crystals. The N¹⁶ is formed by oxygen interacting with neutrons according to the reaction $O^{16}(n,p)N^{16}$. The oxygen concentration was determined by comparing the intensity of the 6.13-MeV gamma-ray photo peak of N¹⁶ from the sample with the same peak from the oxygen standard.

The vacuum fusion analysis was conducted by General Electric Company and an excellent description of this technique has been given by Horton

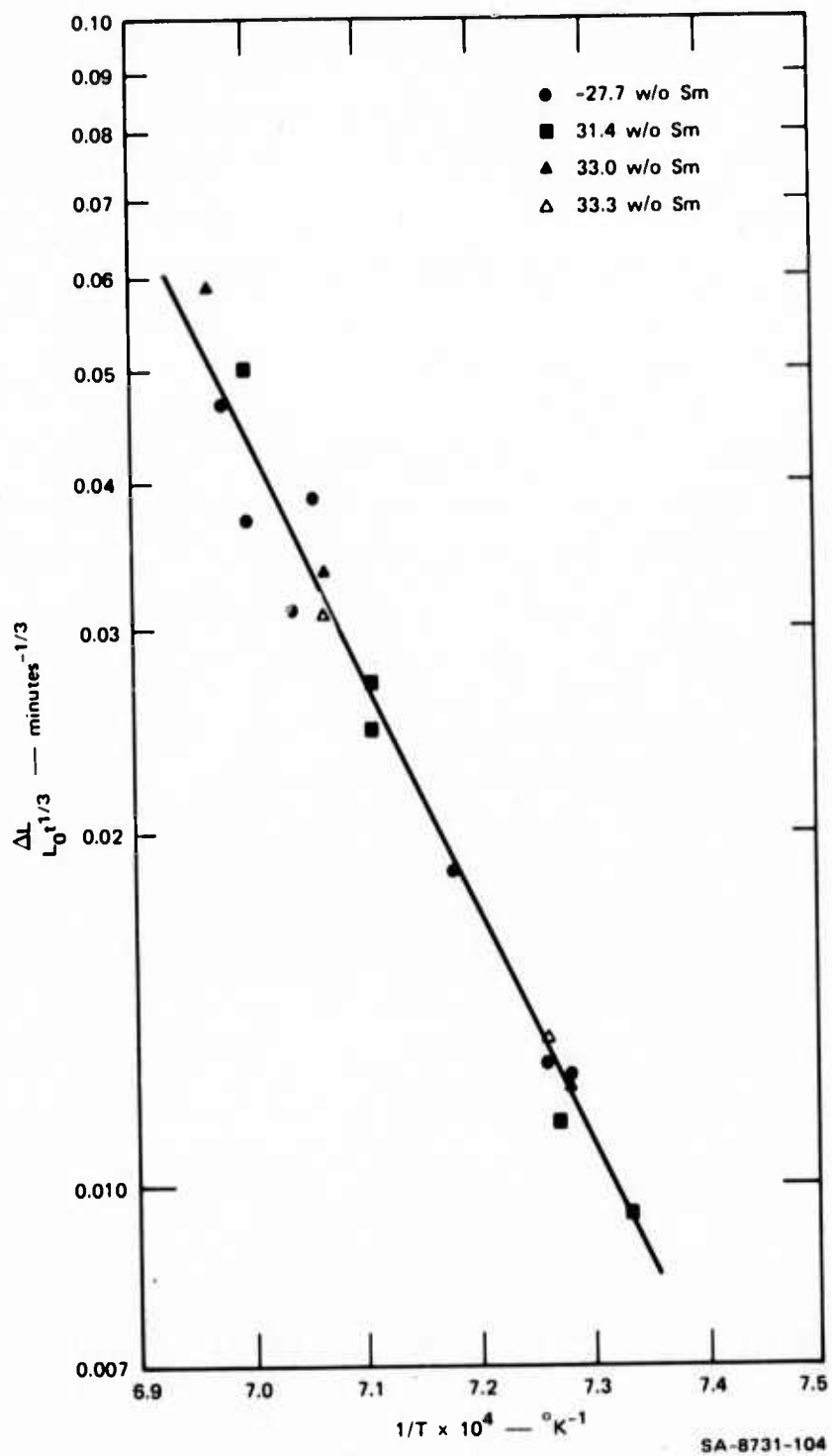


FIGURE 25 ARRHENIUS PLOT OF THE SHRINKAGE RATE VERSUS RECIPROCAL TEMPERATURE

Table 3
OXYGEN ANALYSIS OF SmCo_5 ALLOYS

Alloy No.	Phases Detected by X-Ray Diffraction	Oxygen Concentration (wt%)		Calculated Sm Concentration in Alloy (wt%)	
		Neutron Activation	Vacuum Fusion	Neutron Activation	Vacuum Fusion
M-67	SmCo_5	0.865	1.34	33.3	31.1
M-68	SmCo_5	0.596	1.38	33.0	29.35
M-69	SmCo_5 { $\text{Sm}_2\text{Co}_{17}$	0.544	0.94	31.35	30.1
M-70	SmCo_5 { $\text{Sm}_2\text{Co}_{17}$	0.933	-	27.7	-

and Carson.²³ The technique essentially consists of melting the SmCo_5 alloy in a platinum-tin bath in a vacuum in the presence of an excess of carbon. Carbon monoxide is produced and the amount produced is taken as a measure of the oxygen content in the alloy. The alloy sample is placed in a platinum foil-tin container and introduced into a vacuum side arm above an outgassed graphite crucible containing 95% platinum plus 5% tin held at 900°C in a vacuum of approximately 10^{-5} torr. The sample is dropped onto the solid platinum bath and the temperature is raised to 1950°C requiring approximately 12 minutes to reach 1750°C and approximately 15 to 18 minutes to reach 1950°C . The quantity of gas evolved is determined manometrically using McLeod gages.

Oxidation of powder samples or porous samples may occur during the time the sample resides on top of the platinum bath and this might account at least in part for the higher oxygen values obtained when analyzing by a vacuum fusion technique.

Table 3 also lists the phases detectable by x-ray diffraction. If the oxygen contents determined by vacuum fusion analysis are correct, we would expect that alloy M-68 would contain a greater amount of $\text{Sm}_2\text{Co}_{17}$ than the M-69 alloy. Since this was not confirmed by x-ray analysis, all of the alloys were examined metallographically. M-67 and M-68 contained very small amounts of second phase and M-69 contained much more second phase than did M-68, but less than M-70. Therefore, the x-ray data and metallographic examinations correlate more closely with the neutron activation data. It should be realized that the sintered specimens submitted for oxygen analysis were very porous because only the initial stage of the solid phase sintering process was studied, and the possibility of oxidation occurring during the vacuum fusion analysis does exist.

Additional work is necessary to determine the best method of oxygen analysis in SmCo_5 alloys; however, in this report the neutron activation analysis data have been used to calculate the samarium contents of the

alloys (see Figure 25). The samarium content has therefore been varied almost entirely across the SmCo_5 phase field and into the $\text{Sm}_2\text{Co}_{17}$ phase field with the exception of the postulated hyperstoichiometric SmCo_5 region.²⁴ Since we do not observe any difference in the ratio of shrinkage as the samarium/cobalt ratio is varied, we are forced to conclude that deviations in stoichiometry in this system do not alter the grain boundary defect structure sufficiently to cause a change in the grain boundary transport of the rate-determining species.

Additional work will be completed during the next report period that will allow a quantitative evaluation of the solid phase shrinkage rate, including experiments to extend the samarium/cobalt ratio into the Sm_2Co_7 phase field. This work is necessary before the final conclusions from the solid phase sintering work are made.

REFERENCES

1. P. Kofstad, Nonstoichiometry, Diffusion, and Electrical Conductivity in Binary Metal Oxides, Wiley-Interscience, p. 286, New York, 1972
2. T. L. Felmlee and L. Eyring, J. Inorg. Chem., 1, 660-66 (1968)
3. P. J. Jorgensen and R. W. Bartlett, "Materials Processing of Rare Earth Cobalt Permanent Magnets," Tech. Report AFML-TR-72-225 (September 1972)
4. C. E. Wicks, and F. E. Block, "Thermodynamic Properties of 65 Elements - Their Oxides, Halides, Carbides, and Nitrides," U.S. Bureau of Mines, Bull. 605, Govt. Printing Office (1963)
5. P. J. Jorgensen and R. W. Bartlett, "Materials Processing of Rare Earth Cobalt Permanent Magnets," Tech. Report AFML-TR-72-47 (April 1972)
6. G. D. Stone, Ph.D Thesis, Arizona State University, 1968
7. C. D. Wirkus, M. F. Berard, and D. R. Wilder, J. Am. Ceram. Soc., 50, 113 (1967)
8. M. F. Berard, C. D. Wirkus, and D. R. Wilder, J. Am. Ceram. Soc., 51, 643 (1968)
9. V. B. Tare, and H. Schmalzried, Z. Phys. Chem. N.F., 43, 30 (1964)
10. M. G. Benz and D. L. Martin, J. Appl. Phys., 42, 2786, (1971)
11. J. D. Livingston, "Present Understanding of Coercivity in Cobalt-Rare-Earths, to be published in AIP Conference Proceedings (1972)
12. K. H. J. Buschow, P. A. Naastepad, and F. F. Westendorp, IEEE Trans. Mag. 6, 301 (1970)
13. H. Zijlstra, J. Appl. Phys. 41, 4881 (1970)

REFERENCES (Concluded)

14. M. G. Benz and D. L. Martin, J. Appl. Phys. 43, 3165 (1972)
15. G. C. Kuczynski, Trans. AIME 185, 169 (1949)
16. W. D. Kingery and M. Berg, J. Appl. Phys. 26, 1205 (1955)
17. R. L. Coble, J. Am. Ceram. Soc. 41, 55 (1958)
18. D. L. Johnson and I. B. Cutler, J. Am. Ceram. Soc. 46, 541 (1963)
19. D. L. Johnson, J. Appl. Phys. 40, 192 (1969)
20. K. W. Lay and R. E. Carter, J. Am. Ceram. Soc. 52, 189 (1969)
21. D. L. Johnson, J. Am. Ceram. Soc. 52, 562 (1969)
22. P. J. Jorgensen and R. W. Bartlett, "Materials Processing of Rare Earth-Cobalt Permanent Magnets," Tech. Report AFML-TR-71-188, p. 59 (August 1971)
23. W. S. Horton and C. C. Carson, "Treatise on Analytical Chemistry," Vol. 10, pp 6057-6091, edited by I. M. Kolthoff, P. J. Elving, and E. B. Sandell, Wiley-Interscience (1972)
24. K. H. J. Buschow and A. S. Van Der Goot, J. Less-Common Metals 14, 323 (1968)